



Layered double oxide/copper foam actuates dielectric barrier discharge plasma via electron transport: Exploring the reactive species evolution and diuron disassembly routes

Tianyao Shen^a, Haihe Yu^a, Peng Wang^{a,*}, Xiaojing Wang^c, Chunyan Yang^a, Peng Xu^a, Jianhua Qu^d, Guangshan Zhang^{b,*}

^a State Key Laboratory of Urban Water Resource and Environment, School of Environment, Harbin Institute of Technology, Harbin 150090, PR China

^b Qingdao Engineering Research Center for Rural Environment, College of Resource and Environment, Qingdao Agricultural University, Qingdao 266109, PR China

^c School of Environment, Sichuan Agricultural University, Chengdu 611134, PR China

^d School of Resources and Environment, Northeast Agricultural University, Harbin 150030, PR China

ARTICLE INFO

Keywords:

Dielectric barrier discharge plasma
Layered bimetallic oxide
Diuron
Reactive species
Electron transport

ABSTRACT

Dielectric barrier discharge plasma (DBDP) is a promising advanced oxidation process for water contaminants degradation relying on the coexistence of multiple reactive species. Herein, by introducing carrier foam copper (CuF), a high catalytic activity ternary layered bimetallic oxide (CoFe-LDO/CuF, CFCO) was synthesized. The evolution process (structure-catalytic function) from layered bimetallic hydroxide (CoFe-LDH/CuF, CFHC) to LDO was explored. Phenylurea herbicide diuron (DUR) was efficiently degraded (> 99 %) via the synergistic effects between DBDP and CFCO within 25 min. As an electron transport substrate, CuF promotes the valence circulation (Fe(III)/Fe(II) and Co(III)/Co(II)), guaranteeing the catalysis sustainability and surface Cu₂O helping the generation of reactive oxygen species. The efficacy of multiple active species in DUR disassembly was systematically explored, and the routes of demethylation and deamination are the dominant paths in DUR degradation. The study of synthetic tunable LDO composite, active species reaction, and DUR degradation pathways will expand the applications of DBDP.

1. Introduction

Agriculture supported human survival by providing grains, promoting the population growth and economic prosperity. Due to the intense requirement for agricultural produce, overdose chemical pesticides (herbicides, fungicides, and insecticides) have been input into the environment to control pests and weeds seeping into the soil and flowing into rivers [1]. Various pesticides, especially herbicides, were detected in worldwide surface water [2,3]. Characters of structural stability and ecotoxicity make herbicides possess a potential risk to the ecological environment and biological health [4,5]. The advanced oxidation processes (AOPs), with the advantages of versatility and efficacy in decontamination, were rightfully regarded as a reliable ally in herbicide removal [6].

As an emerging AOP, depend on generation technology, discharge plasma technology makes it possible for various active species (O₃, H₂O₂, •OH, •O₂⁻, and e⁻/•H, etc.) to co-exist [7]. Dielectric barrier

discharge plasma (DBDP) belongs to the non-thermal plasma, whose treatment process temperature monolithic stability, and the cooling device is unnecessary. Unlike other plasma technologies, the dielectric barrier made the discharge evenly, extending the electrode service life and elevating reaction efficiency in DBDP [8,9]. Under the input of a high voltage, the current breaks through the gas-liquid interface, active species expand, synergy generates in different pathways, and pollutants could be degraded in DBDP systems with lower electric current [10]. Various methods, including catalyst assisted, add extra oxidants or modify the plasma reaction device to enhance the reaction efficiency of DBDP [11–13]. Regrettably, these researches focus on revealed the coexistence of multiple active species improved the degradation performance, but the interactions among different pollutants/active species for improvement of performance is still unclear [14]. Thus, under the circumstance of multiple active species constituents, the integration of oxidative mechanisms and optimization of oxidants utilization in novel electrochemical systems deserve an in-depth study.

* Corresponding authors.

E-mail addresses: pwang73@hit.edu.cn (P. Wang), gszhang@qau.edu.cn (G. Zhang).

<https://doi.org/10.1016/j.apcatb.2023.122950>

Received 27 March 2023; Received in revised form 11 May 2023; Accepted 31 May 2023

Available online 2 June 2023

0926-3373/© 2023 Elsevier B.V. All rights reserved.

Layered double hydroxide ($[M_1^{2+}_x M_2^{3+}_x (OH)_2 (A^{n-})_{x/n}]^{x+}$, LDH), a class of bimetallic hydroxide materials hydrotalcite-like compounds, belong to a large two-dimensional (2D) anionic clay family [15]. Various metals combination could be incorporated into the LDH structure for different purposes. Hence, based on the structure character advantages, LDH has been widely applied from drug delivery to environment depollution and electrode catalysis [16–18]. Layered double oxide (LDO) is a metal oxide obtained by LDH calcination, which has a more stable structure and is suitable for water environment decontamination [19]. Especially, due to calcination exposure to the basic centers, LDO has strong Lewis base sites than LDH [20], and better serves as an electron donor. Previous studies have largely focused on the physico-chemical properties, the lamellar structure, and some applications in different industrial fields [21–23]. However, little attention has been paid to the micromorphology evolution under the thermal process and the structure interfaces effect in the heterogeneous Fenton-like catalytic activity for organic pollutants removal.

This work investigates the synergistic decomposition of Diuron (DUR) between the DBDP process and LDO, emphasizing the synthesis conversion process of CoFe-LDH \rightarrow CoFe-LDO. Make up for the absence of the study on LDH/LDO structure and LDO application as environmental functional catalysts. Not only that, the powder CoFe-LDO was immobilized by using copper foam (CuF) as a carrier. The synergistic effect between CoFe-LDO/CuF (CFOC) and DBDP was revealed. Clarification of the reactive oxygen production (ROS) mechanisms and identification of the active species' production paths were both conducted. In addition, combined with density functional theory (DFT) calculations, the possible degradation pathways of DUR were systematically and comprehensively analyzed, including intermediate product composition, bonds cleave location and system ecotoxicity. This work would be conducive to the development of DBDP technology on eco-friendliness, high efficiency, and sustainable direction, gradually practical applications.

2. Experiment

2.1. Materials

All chemicals and reagents were of analytical grade and deionized (DI) water was used throughout the experiments. Details are shown in Text S1.

2.2. Synthesis of CoFe-LDH, CoFe-LDO, and CoFe-LDO/CuF

Hydrothermal-calcination method was used to synthesize CoFe-LDO/CuF. The precursor (CoFe-LDH/CuF) was composited via hydrothermal procedures: pieces of CuF (10 mm \times 10 mm \times 1 mm) were immersed into a homogeneous mixed aqueous content 0.1 M $Fe(NO_3)_3 \cdot 9H_2O$, 0.3 M $Co(NO_3)_2 \cdot 6H_2O$ and appropriate urea; the mixture was transferred to a tetrafluoro-lined hydrothermal kettle and maintained the temperature at 120 °C for 18 h; the deposits were washed alternately with DI water and ethanol, labeled as CFHC.

The final composite was obtained by calcination. The precursor CFHC was placed into a tube furnace and calcined at 460 °C for 2 h, and the product (CoFe-LDO/CuF) was labeled as CFOC.

Except for adding CuF, powdery LDH-LDO series materials were prepared in the same procedure as CFOC. Powder products obtained at different calcination conditions (uncalcined, 300 °C, 380 °C, 460 °C, 540 °C, and 620 °C) temperatures are labeled as LDH, LDO300, LDO380, LDO460, LDO540, and LDO620.

2.3. Characterization of catalysts

Thermogravimetric Analysis-Mass spectrometry (TGA-MS, STA449F5, Netzsch) tested the conversion of the material under the thermal effect. The transmission electron microscope (TEM, JEM-2100,

JOEL), X-ray diffractometer (RD, D8 Advance, Bruker), and scanning electron microscope with Energy Dispersive Spectroscopy (SEM&EDS, Sigma500, Zeiss) were applied to characterize the morphological characteristics. The Brunauer-Emmett-Teller (BET) specific surface area was detected by N_2 adsorption-desorption isotherms with an automatic surface area and porosity analyzer (QUADRASORB SI, Quantachrome). Surface vacancies were detected by the electron spin resonance spectrometer (ESR, ESP-300E, Bruker). The surface functional groups were detected by Fourier transform infrared spectrometer (FTIR, Spectrum One, PerkinElmer). X-ray photoelectron spectroscopy (XPS, ESCALAB 250Xi, Thermo Fisher) provided the chemical information of catalysts. The electrochemical performance of electrochemical impedance spectroscopy and linear sweep voltammetry were tested using an electrochemical workstation (EIS&LSV, CHI660E, Chenhua).

2.4. Experimental procedure

The experimental device was a coaxial cylindrical DBDP reactor (Fig. S1). The detailed experimental procedures of DBDP/CFOC to remove DUR are as follows: i) Inject 200 mL of 10 mg L^{-1} DUR-containing simulated polluted water into the reaction container while turning on the water (150 mL min^{-1}) and gas circulation (1.5 L min^{-1}). ii) Immerse the catalysts in the reaction container until the discharge area and the reaction container reaches the complete gas-liquid homogeneous; iii) Adjust the input voltage to be stable, then time counting starts immediately, and withdraw samples at 5 min intervals with discharge voltage stable until the last sample is taken (25 min). iv) Continue for 25 min, turning off the power supply, and a batch of experiments was finished. Sole-DBDP experiment was carried on without CFOC addition and solo-CFOC experiment was carried on without the voltage input, other steps were exactly the same as that of DBDP/CFOC.

2.5. Analytical methods

The samples collected in the experiment were detected with a high-performance liquid chromatography (HPLC, Agilent 1290) equipment with a C18-P column (5 μm , 4.6 \times 150 mm) and an ultraviolet detector with a detection wavelength of 254 nm. Based on the HPLC detection, DUR removal efficiency (η) was calculated as Eq. (1):

$$\eta(\%) = \frac{[DUR]_0 - [DUR]}{[DUR]_0} \times 100\% \quad (1)$$

where $[DUR]_0$ and $[DUR]$ are the initial and time t concentration of DUR, respectively (mg L^{-1}).

Input power is calculated according to the Eq. (2):

$$P_w = f C_n A \quad (2)$$

where the frequency f is measured by the oscilloscope, C_n is the sampling capacitance (with A value of 1 μF), and A is the area of the Lissajous-Figure.

The energy efficiency is calculated as shown in the Eq. (3):

$$G_{50} = \frac{0.5 \times m}{P \times t_{50}} \quad (3)$$

where m is the initial mass of the pollutant (mg), P is the discharge power (W) and t_{50} is the time required for the degradation of 50 %.

The Hindrance efficiency ξ (%) of the scavenger agents on DUR elimination is calculated as Eq. (4):

$$\xi(\%) = \frac{k_0 - k}{k_0} \times 100\% \quad (4)$$

where k_0 is the degradation rate without the scavenger agents (min^{-1}), and k is the Quasi-first-order dynamics with the addition of scavengers (min^{-1}).

2.6. DFT calculation method

The PBE functional was used in the DFT Part. Slab surface unit cells with dimensions $3.75 \text{ \AA} \times 3.75 \text{ \AA} \times 3.75 \text{ \AA}$ for Cu and $4.30 \text{ \AA} \times 4.30 \text{ \AA} \times 4.30 \text{ \AA}$ for Cu_2O were built using experimental bulk-cubic lattice parameters. Cleave along the crystal surface with the strongest diffraction intensity (1 1 1), and the vacuum slab thickness was 15 \AA . Fukui function calculations were utilized to analyze the degradation pathway of DUR.

3. Results and discussion

3.1. Crystal structure, morphology and physicochemical properties

The corresponding oxide composites were obtained from the calcined precursor LDH. To monitor the microscopic transformation process, the morphology and thermogravimetric mass at different calcination stages were analyzed (Fig. 1). The initial biscuit-like LDH lamellar structure could be maintained below 300°C (Figs. 1b to 1c), and the tiny weightlessness at this stage may be due to the evaporation of water from the material's surface. As the temperature continued rising, lamina adhesion formed to thick lamellar, with the onset of exothermic crystalline transformation (Figs. 1c to 1d). The second weightless step, the main stage, was from 380°C to 460°C . Layer spacing disappears, and a blocky structure appeared instead (Figs. 1d and 1e), which is presumably due to the dehydroxylation process. Simultaneously CO_3^{2-} also escape in the form of CO_2 (Fig. 1a). The endothermic peak located at 300°C – 460°C , during which stage the first crystallization transformation is completed. Figs. 1h and 1i displayed the TEM image of LDH and LDO460, whence an observationally

predicted that the thin transparent layer transforms into multiple layers of overlapping black. The last stage was above 500°C , in which the structure $-\text{OH}$ and interlayer CO_3^{2-} had completely escaped, and pores appeared on the block surface until the bulk disintegrated (Figs. 1f and 1g). The endothermic process continues, widely accepted reason for this endothermic was that it began the next oxidation stage. To further confirm the composition of the series material, the XRD pattern and FTIR spectrum are shown in Fig. S2. As depicted, $-\text{OH}$ vibration around 3400 cm^{-1} and peaks (1500 cm^{-1} and 700 cm^{-1}) assigned to CO_3^{2-} appeared in LDH [24]. With the increase of calcination temperature, the peaks of $-\text{OH}$ and CO_3^{2-} faded away (Fig. S2b), and the CoFe bimetallic hydroxide evolved into bimetallic oxide (Co_3O_4 and FeOOH , Fig. S2a), which could exhibit excellent radical ($\bullet\text{OH}$) generating ability in AOPs [25,26]. Peaks attributed to CoCO_3 (25.0° , 32.6° , and 53.8°) could be found in LDH, but fade away with the calcination temperature increase, which further confirmed the escape of CO_3^{2-} . The influence of high temperature on the specific surface area of LDOs was studied by N_2 -adsorption/desorption isotherms. As shown in Fig. S3 and Table S1, combined with SEM, speculating that the gradual collapse of the structure might reduce the surface area. When the block was completely disintegrated (620°C), specific surface area increased with the pore and agglomeration particles on the surface. The integrated characterization comprehensively demonstrated the evolution of $\text{LDH} \rightarrow \text{LDO}$. Generally, the transformation process was summarized as follows: i) The hydrothermally synthesized precursor consists of layered hydroxyl bimetallic oxides (CoFe-LDH) and interlayer CO_3^{2-} connected with cationic plate; ii) Thermal environments caused $-\text{OH}$ and CO_3^{2-} in the LDH structure escaping as H_2O and CO_2 , the layer spacing were gradually reduced, and metallic element converted to metal oxide (Co_3O_4 and FeOOH).

To improve performance and recyclability, the powder anchored on

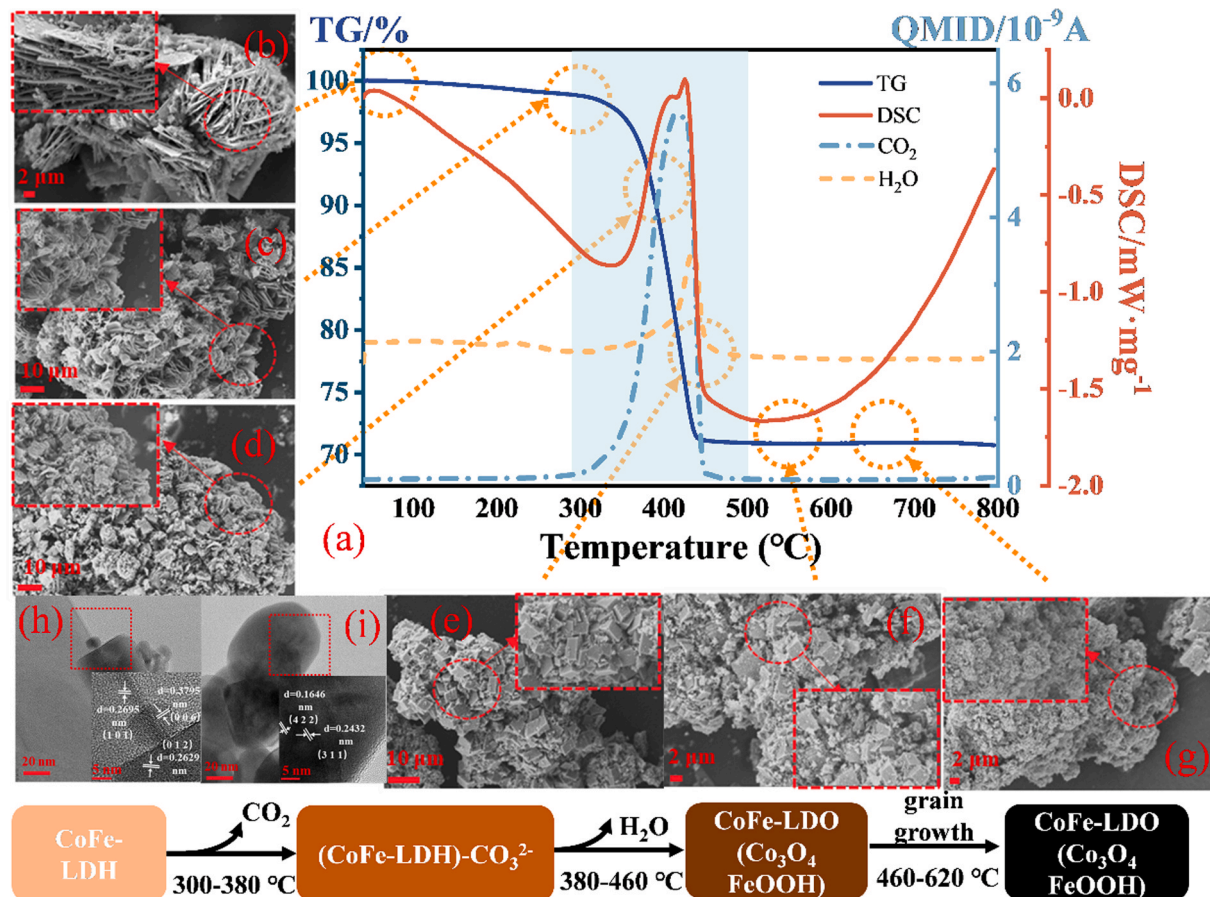


Fig. 1. TGA image of LDH→LDO (a), SEM image for LDH (b), LDO300 (c), LDO380 (d), LDO460 (e), LDO540 (f), and LDO620 (g). TEM image of LDH (h) and LDO460 (i).

the CuF surface forms a ternary catalyst. SEM-EDS and TEM further investigated the size and micromorphology of CuF, CFHC, and CFOC in Fig. 2. CuF mainly exists as a reticular structure (Fig. 2a) with an average branch width of about 50 μm . Obviously, these branches are sufficient to support the grains loaded. The thin layer and square sheet composing a bud structure of CFHC were confirmed in Figs. 2b and 2c. Fig. 2c exhibited the detailed morphology of CFHC, revealing LDH sheets with nanometer thickness. Unlike binary LDH, CFHC had a smoother and thinner surface, implying Cu ion might involve in the construction of surface catalyst. Characterizations of synthesized CFOC are shown in Figs. 2d-2j, including surface morphology, structure size, and element distribution. Due to the escape of CO_2 and H_2O , the layer spacing decreased, the thin layer structure faded away, and relatively thick oxide sheet blocks were formed on the surface of CuF (Figs. 2d and 2e). O, Fe, Co, and Cu are distributed uniformly on the surface of CuF branches (Figs. 2f-2j). More detailed microstructural information on CFOC was obtained via TEM and HRTEM (Figs. 2k-2m). The squares, with an average side length of about 20 nm, are stacked randomly stack-up (Fig. 2k). Clear atomic lattice fringes can be observed in Fig. 2l. The crystallographic lattice spacing measurement is shown in Fig. S4. Refer

to JCPDS: 74-2120 (Co_3O_4) and JCPDS: 78-2076 (Cu_2O), suggesting the carrier Cu participated in the oxidation reaction and was partially converted to Cu_2O . The corresponding exposed crystal faces are distinguished (Figs. 2l and 2m), which are similar to those from XRD, illustrating that the LDH on the composite surface converted to LDO after calcined.

The crystallographic structure and phase of LDH, CFHC, LDO460, and CFOC were detected by XRD in Fig. 3a. The intensity diffraction peak locating at 43.32° (1 1 1), 50.45° (2 0 0) and 74.12° (2 2 0) well correspond to the cubic Cu (JCPDS: 85-1326), which possessed the high strength concealing the diffraction peak of the surface load. As for bare LDH, the diffraction peaks located at 23.42° (0 0 6), 34.08° (0 1 2), and 38.73° (0 1 5) are readily indexed to the CoFe-LDH (JCPDS: 50-0235). The combination of interlamellar anions with lamellar cations to form CoCo_3 could be identified by comparison with JCPDS# 11-0692. These diffraction peaks could be observed at the enlarged XRD pattern of CFHC, suggesting the crystallinity of LDH nanosheets' presence on the CuF micro-reticulate surface, which could also be confirmed from SEM. A similar phenomenon occurred in LDO460 and CFOC. To weaken the influence of the strong diffraction peak of cubic Cu, the XRD diffraction

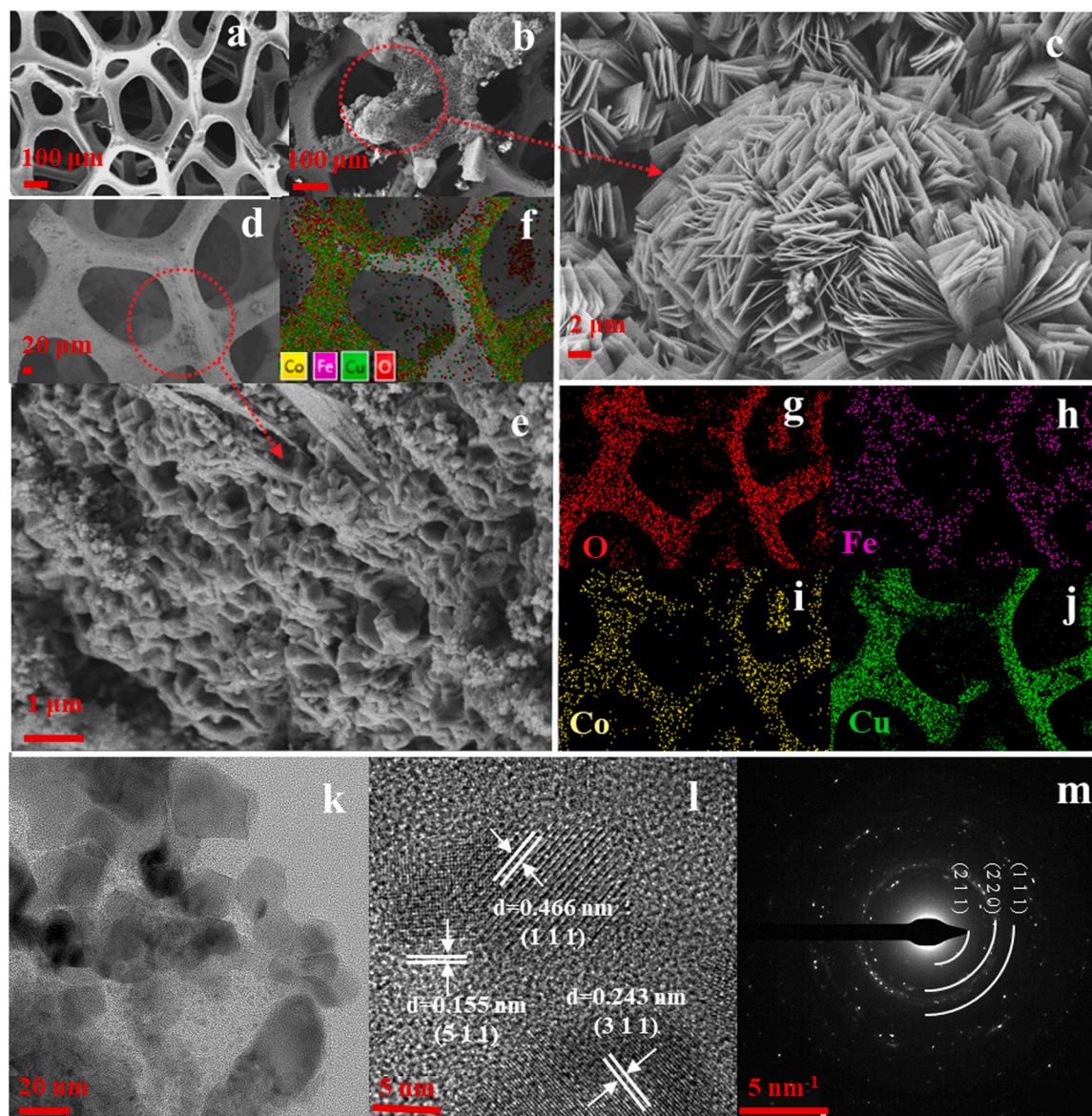


Fig. 2. SEM image of CuF (a), CFHC (b), CFHC (enlarged) (c), CFOC (d), CFOC (enlarged) (e). EDS image of CFOC for O, Fe, Co, and Cu scanning (f)-(j). TEM, HRTEM and SAED image for CFOC (k)-(m).

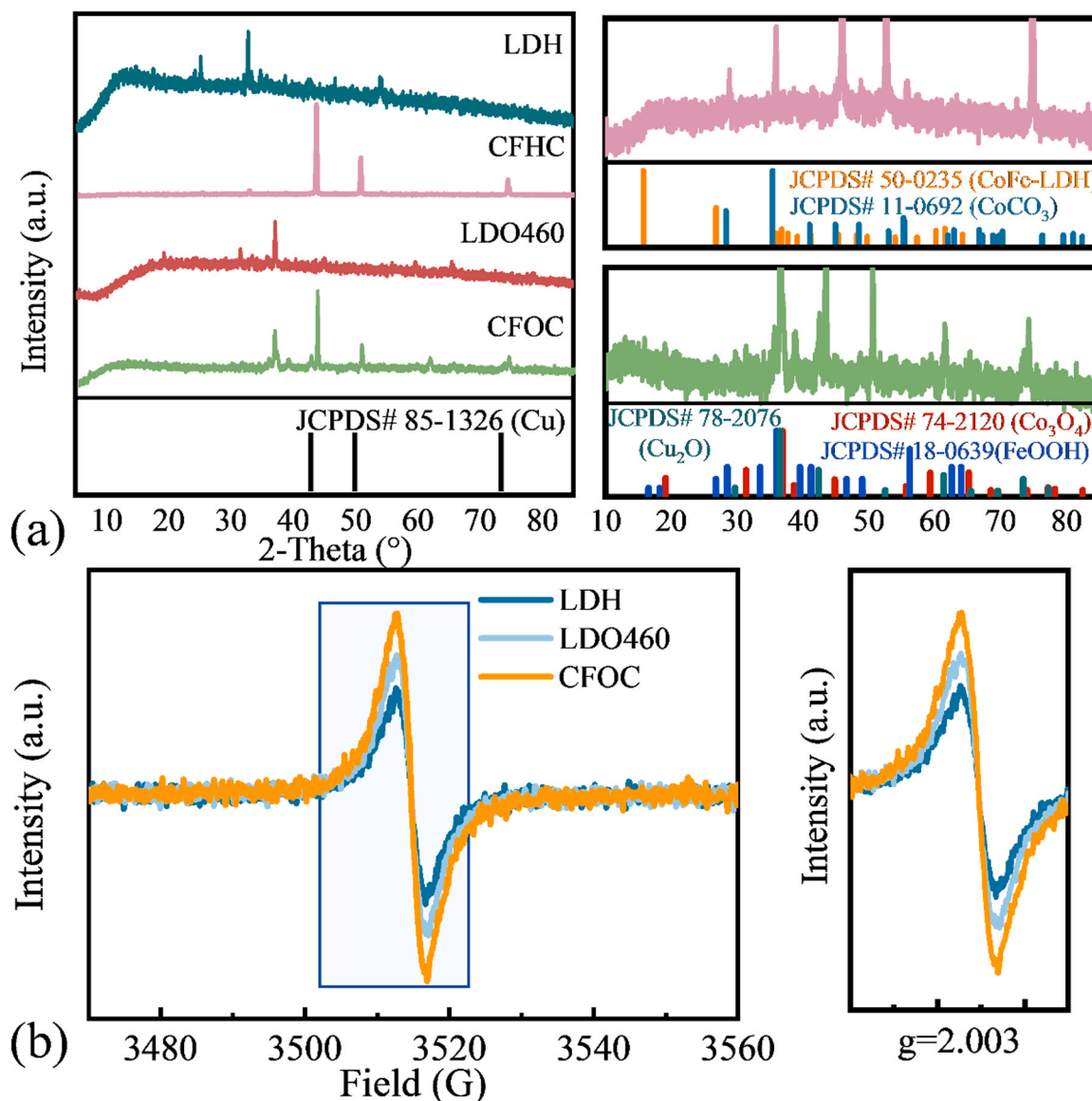


Fig. 3. XRD patterns (a) of LDH, CFHC, LDO460, and CFOC; EPR spectra (b) of LDH, LDO460, and CFOC.

pattern has been partially enlarged. The diffraction peaks of Co₃O₄ (JCPDS: 74-2120) located at 18.99° (1 1 1), 31.27° (2 2 0), 36.84° (3 1 1), and FeOOH (JCPDS: 18-0693) peaks at 35.89° (2 1 1), 41.18° (0 3 1), 62.63° (0 0 2) were observed in LDO460 and CFOC (enlarged Figure). Especially, the diffraction peaks belong to Cu₂O, 36.44° (1 1 1), 42.32° (2 0 0), and 73.55° (3 1 1) arise in the XRD diffraction of CFOC. XRD and TEM arrived at the same conclusion that the matrix CuF participated in the formation of a surface catalyst. As depicted in Fig. 3b, there is a symmetrical EPR signal at $g = 2.003$, confirming the existence of oxygen vacancies (O_v) [27]. CFOC displayed the strongest signal in the prepared catalysts, indicating the existence of more abundant O_v contents because of the promoting effect of calcination and CuF on the generation of surface defects.

The effect of the CuF supporter on the S_{BET} of the catalyst is shown in Fig. 4a. Apparently, CuF has a negative impact on the S_{BET}, which could be attributed to the fact that the macroporous structure in the foam network of CuF could not be accurately measured and the loading amount limit the S_{BET}. Besides, the isotherm curves of LDO460 and CFOC were categorized as typical IV curves with a type H3 hysteresis loop (IUPAC classification), confirming the existence of mesoporous in catalysts, which corroborated by the average pore diameter detection

(37.19 nm and 35.55 nm for LDO460 and CFOC, Table S2). FTIR (Fig. 4b) presented variations of functional groups of prepared catalysts. The -OH (3452 cm⁻¹) and CO₃²⁻ (1500 cm⁻¹) strong stretching vibrations peaks in the LDH are absent in the infrared absorption spectrum of LDO460 and CFOC [28]. The weakening of the absorption peak implies the existence reduction of oxygen-containing groups. The peaks around 690 cm⁻¹ and 560 cm⁻¹ in LDO460 and CFOC originated from the stretching vibration of M-O (M = Fe/Co) [29]. Except for a slightly stronger M-O absorption peak, there was no noticeable difference in the infrared spectrum of CFOC and LDO460, which might be attributed to the increase of Cu-O bonds [30]. The inherent electrochemical properties of the catalysts are essential to the electron-transfer process, and EIS was used to estimate the conductivity (charge-transfer capacity). In the Nyquist plots shown in Fig. 4c, CFOC exhibited the smallest radius, reflecting less resistance during electron transfer. A smaller radius might improve catalytic performance since oxidants and pollutants could more readily transfer electrons at the CFOC interface. Fig. 4d shows significant differences in the CV curves of powder catalysts (LDH and LDO) and pieces CFOC. As a result of the Cu support, the reduction peak current increased to 0.41 mA, suggesting that the activity of the CFOC was enhanced with Cu. Electrochemical test results hint at the possible

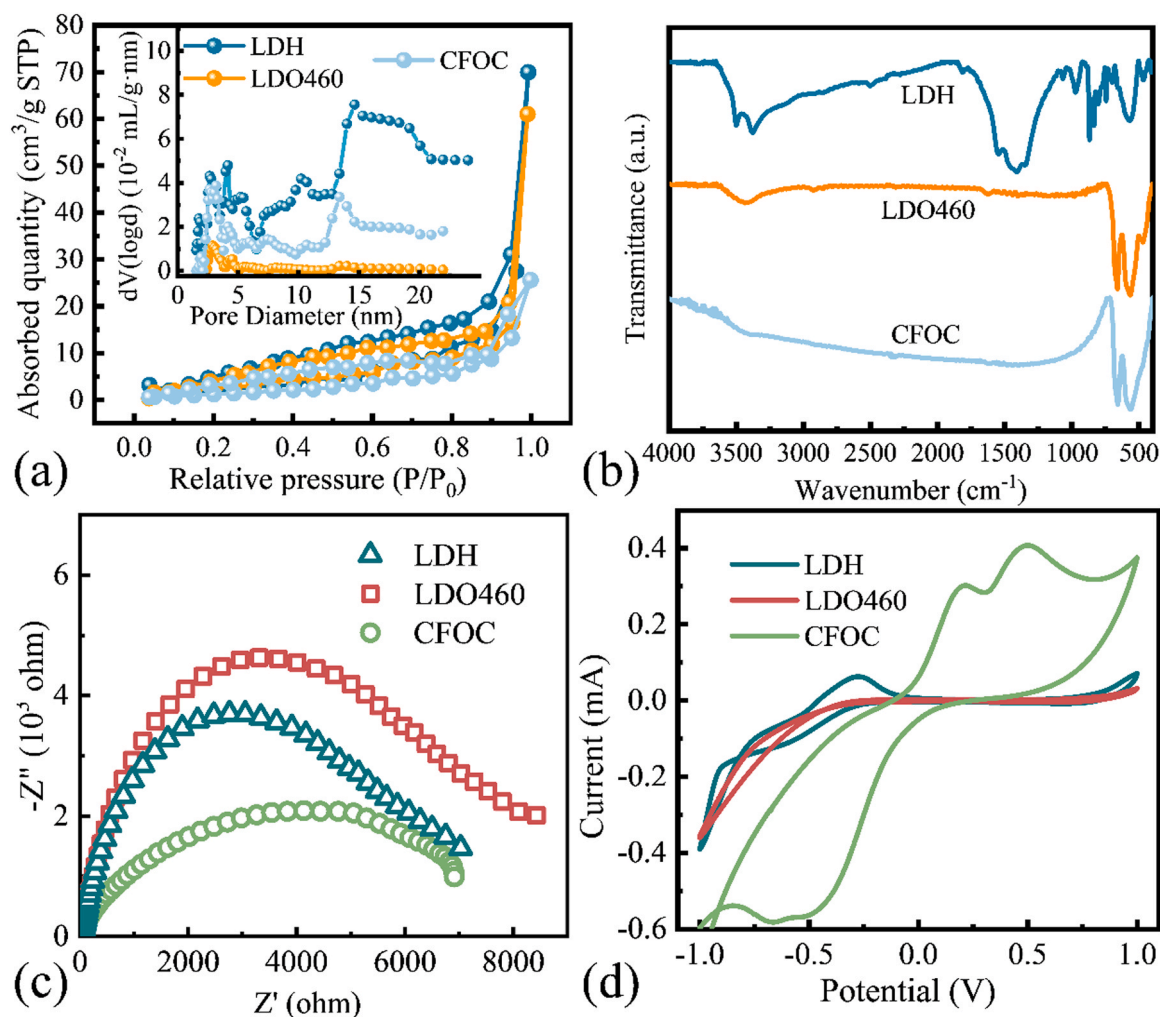


Fig. 4. N₂-adsorption-desorption curve and the distribution of pore size (inset) (a), FTIR spectra (b), EIS (c), and CV (d) of LDH, LDO460, and CFOC.

catalytic potential of CFOC.

For comparison, XPS characterizations were performed to display the composition of elements and valence. As shown in Fig. S5a, Co, Fe, and O were detected for all the investigated samples, and additional Cu was detected in CFOC. Fig. S5b displays the high-resolution Fe 2p XPS spectra of LDH, LDO460, and CFOC, well-fitted into 2 peaks attributed to Fe 2p_{1/2} and Fe 2p_{3/2}. The fitting peaks centered at 711.2 eV and 713.5 eV are assigned as Fe²⁺ and Fe³⁺, respectively [31,32]. Calcination and composite reduced the content of Fe²⁺ but increased the proportion of Co²⁺ (Table S3), signifying that the electron flow is from Fe to Co. As shown in Fig. S5c, the fitting peaks around 780.1 eV and 795.8 eV could be assigned to Co 2p_{1/2} and Co 2p_{3/2}, respectively. From the high-resolution XPS spectra of Co 2p, the main peaks of Co²⁺ and Co³⁺ are located at 781.9 eV and 779.6 eV [33]. Calcination has an insignificant effect on the content of metal elements (Fe and Co), but the further loading on CuF reduced the amount of Fe and Co detected. These phenomena are reasonable because those metallic elements remained solid at 460 °C, but the composites limit the surface particle content. The asymmetrical O 1s spectra of these samples could be deconvoluted into three components at 529.5 eV, 531.4 eV, and 532.7 eV, respectively corresponding to lattice oxygen (O_L), surface adsorption oxygen (O_{abs}), and surface hydroxyl groups (–OH) [27,32]. The combination with CuF significantly increased the content of O_A (from 24 % to 43 %), which is derived from dissociative oxygen on O_V and represents the amount of O_V, benefiting catalytic efficiency promotion [34,35]. The high O_A content of CFOC is consistent with the ESR detection results that the

introduction of low valence reduction metal support increased the activity of the catalyst.

3.2. DUR degradation and application evaluation of DBDP/CFOC system

In previous investigations, LDH and LDOs have been applied in DBDP catalysis to eliminate DUR. The degradation efficiency, kinetics, and ionic dissolution are shown in Fig. S6 and Table S4. Compared with low temperature calcination (≤ 380 °C), LDO460 has relatively better stability and catalytic performance, which might be because that calcination helps stabilize metal ions and metal oxide conversion. According to characterization, after 460 °C calcination, LDH has completed the dehydrating and removing the interlayer anions steps, converting to LDO. Continue elevating calcination temperature just increase the energy-consumption, but had no use on the catalytic performance improvement. The performance of catalysts in the DBDP process was comprehensively exhibited in Figs. 5a and 5b. The sole DBDP process had a limited removal effect on DUR elimination (< 80 %); by contrast, DUR removal efficiency was clearly elevated by introducing LDH or LDO460 into the DBDP process to about 95 %. Due to CuF providing the reduced state copper, more oxygen vacancy and active sites participated in DBDP catalyzing. Furthermore, the excellent conductivity of CuF significantly reduced electron transport resistance. Based on these characteristics, the composite of the powder catalyst and CuF significantly accelerated the degradation process of DUR. Compared with LDO460, the degradation rate of DUR in CFOC/DBDP increased to 1.9

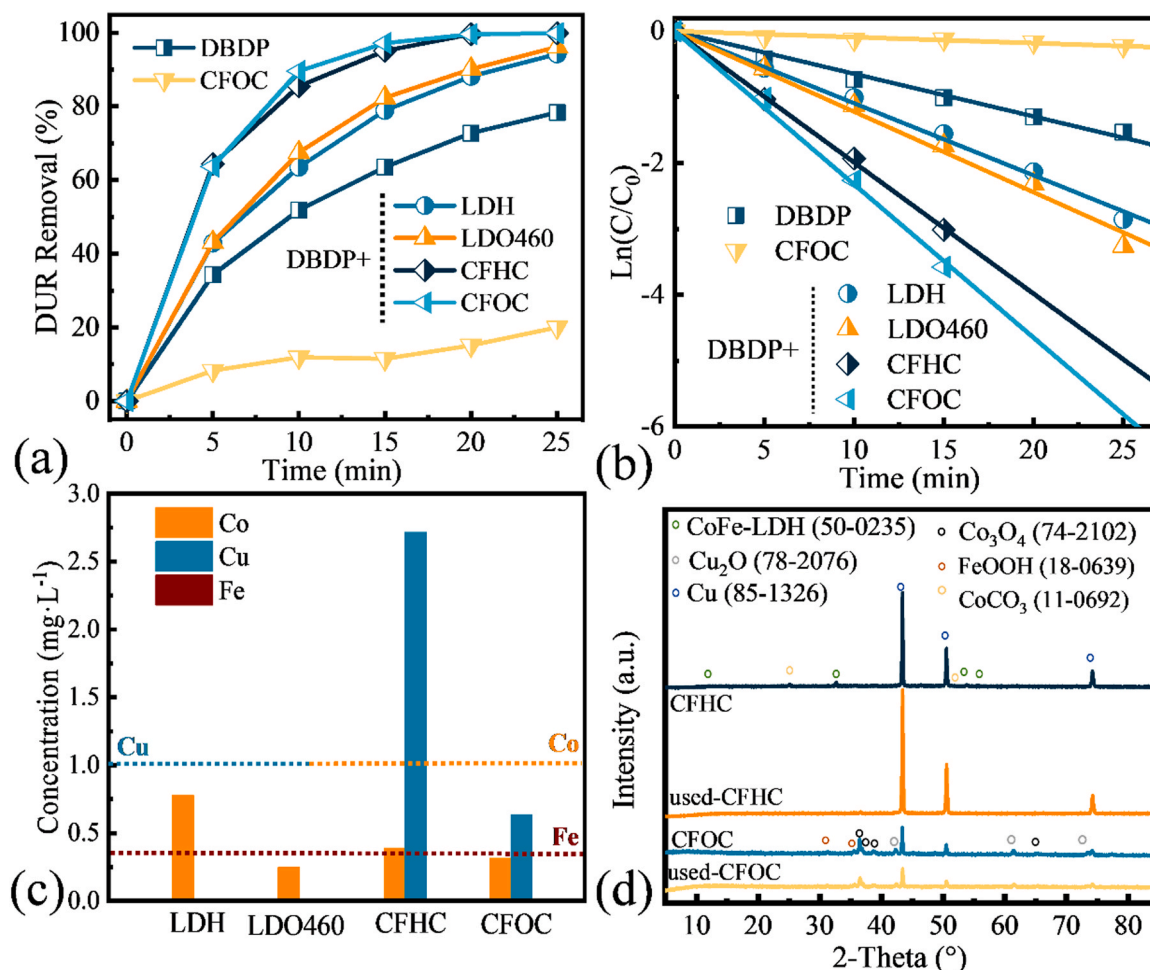


Fig. 5. DUR degradation efficiency (a) and rate (b) under different oxidation process. Ion leaching concentration (c) and XRD pattern (d) of different catalysts.

times (0.1221 min^{-1} for DBDP/LDO460 and 0.2324 min^{-1} for DBDP/CFOC). Sole-CFOC could not remove DUR efficiently, but the $\sim 100\%$ DUR removal efficiency was achieved via the synergistic action of DBDP and CFOC. Following Eq. (5) [36], the calculation result of synergistic intensity was 3.41, confirming the existence of synergies.

$$\text{Synergistic intensity} = \frac{k_{\text{DBDP/CFOC}}}{k_{\text{DBDP}} + k_{\text{CFOC}}} \quad (5)$$

where $k_{\text{DBDP/CFOC}}$, k_{DBDP} and k_{CFOC} (min^{-1}) were the apparent pseudo-first order reaction rate constants of DUR degradation for DBDP/CFOC, sole-DBDP and sole-CFOC systems.

The similar catalytic capacity of CFOC and CFHC could be attributed to the same composite of metallic elements. However, calcination ended CFOC with better stability than CFHC. As shown in Fig. 5c, $2.72 \text{ mg}\cdot\text{L}^{-1}$ Cu ions were detected in DBDP/CFHC-purified water, which was above the environmental quality standards for surface water (GB3838-2002, China). High ion leaching suggests the instability of CFHC and potential metal ion contamination risk. XRD patterns of fresh and recycled catalysts obtained similar results in Fig. 5d. The diffraction peak of LDH seems to have disappeared on the recovered CFHC surface, but the tiny peaks of LDO still locate on the surface of the recovered CFOC. Therefore, although both materials can effectively combine with DBDP to remove DUR, from the perspective of material stability, CFOC is more suitable for the DBDP process.

Generally, different discharge powers produce plasma impact the electron densities, affecting DUR removal in water. The Lissajous-Figure graphic is shown in Fig. 6a, and the corresponding input voltage waveforms are displayed in the inset, where the power consumption

calculated by combining Figures and Eq. (2) are marked in different colors. Fig. S7a exhibits the evolution of DUR removal efficiency with time under different input power. When the input power was higher than 3.02 W (16 kV), the DUR removal reached reaction equilibrium at 15 min, and the removal rate was calculated by intercepting the data of the first 15 min (Fig. S7b). Fig. 6b comprehensively compares the effect of the input power on the DUR degradation. From 0.59 W to 3.02 W , the removal efficiency and rate of DUR significantly increased with adjusting the discharge power up, and from 3.02 W to 5.68 W , the increase rate slowed down. The highest energy yield of DUR degradation was $0.11 \text{ mg}\cdot\text{W}^{-1}\cdot\text{min}^{-1}$ at 3.02 W , indicating that energy input could improve DUR removal efficiency, but the application should consider the optimal energy utilization.

Water matrices affect pollutants elimination via different coexisting substances, and these effects were investigated in Figs. 7a-7d. DI water, tap water (Mobanshan Reservoir, 110.6°E , 24.5°N), and river water (Songhua River, 126.5°E , 45.8°N) were accessed to prepare simulated DUR sewage. Varying degrees of adverse influence of tap water and river water in DUR elimination appeared in Figs. 7a and 7b. The DUR removal efficiency in tap water and river water decreased to 86.9% and 75.6% , and the removal rate dropped to 0.076 min^{-1} and 0.054 min^{-1} , respectively. As shown in Table 1, Figs. 7c and 7d, this phenomenon could be summed up in reasons from two aspects: the influence of coexisting organic matter and coexisting anions. UV_{254} is the absorbance in water at 254 nm , reflecting the amount of natural organic matter (humic macromolecular organic matter and aromatic compounds, NOM) containing $\text{C}=\text{C}$ and $\text{C}=\text{O}$ that naturally exist in water. As displayed in Fig. 7c, while the processing time was prolonged, the ultraviolet

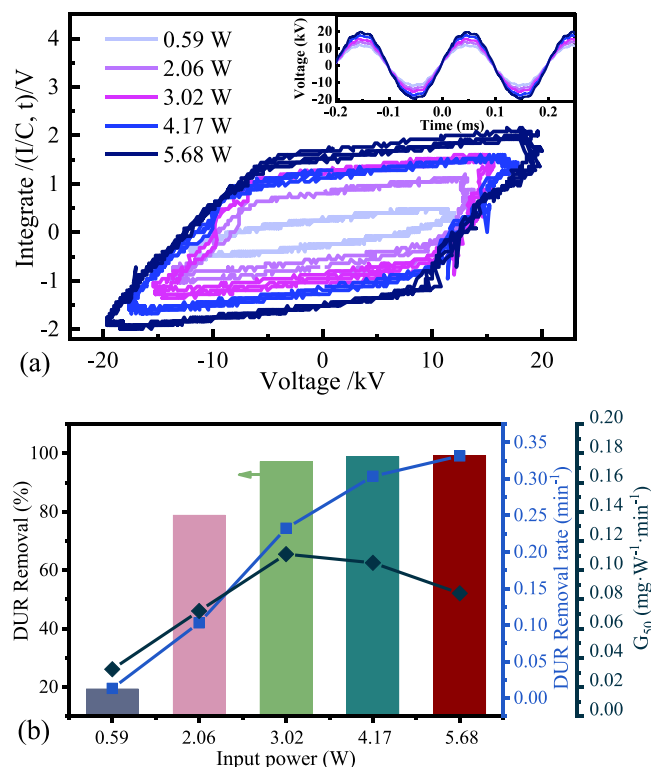


Fig. 6. The image of the voltage wave (inset) and Lissajous-Figure (a). The power effect on DUR elimination, removal rate, and G_{50} (c).

absorption of organic matter was continuously reduced, declaring that both NOM and DUR were degraded simultaneously. 230–270 nm is the characteristic absorption band of aromatic compounds, which is an

absorption band produced by the vibration of the benzene ring and the transition of the closed circular conjugated double bond $\pi \rightarrow \pi^*$. The weakening of absorption peaks in Fig. 7d in various water substrates indicates that the stable aromatic structure was destroyed. Thus, the high content of NOM suppresses the degradation of DUR via competition. The impact of coexisting anions is mainly due to the combination with reactive oxygen species (ROS) to transform into weak oxidizing radicals, affecting the entire oxidation capacity [36,37]. Especially, in our previous study, different concentrations of Cl^- have an adverse impact on the DBDP system [10].

The reusability and stability were tested via reutilization experiments and ion dissolution concentration detection. Cycling experiments were conducted five times and depicted in Fig. 7e. The DBDP and recycled CFOC maintained excellent pollutant removal capacity (> 98 %) after five complete discharge procedures. Low-concentration ion leaching suggests the stability and safety of CFOC. In the course of multiple uses, these ion element concentrations met the safety standards for water quality (Cu and Co 1.0 mg·L⁻¹, Fe 0.3 mg·L⁻¹, GB3838–2002, China), and the outstanding stability of the catalyst is consistent with the XRD detection. Generally, DBDP/CFOC performed well in the stability and security of the practical applications.

Table 1
Water quality parameters.

	DI water	Tap water	River water
Cl^- (mg L ⁻¹)	0.52	3.59	16.07
SO_4^{2-} (mg L ⁻¹)	0.43	6.63	20.02
NO_3^- (mg L ⁻¹)	0.31	4.03	6.71
TOC (mg L ⁻¹)	0.94	6.26	36.19
pH	6.76 ± 0.02	7.02 ± 0.02	7.65 ± 0.02
Temperature (°C)	18.2	15.4	18.7

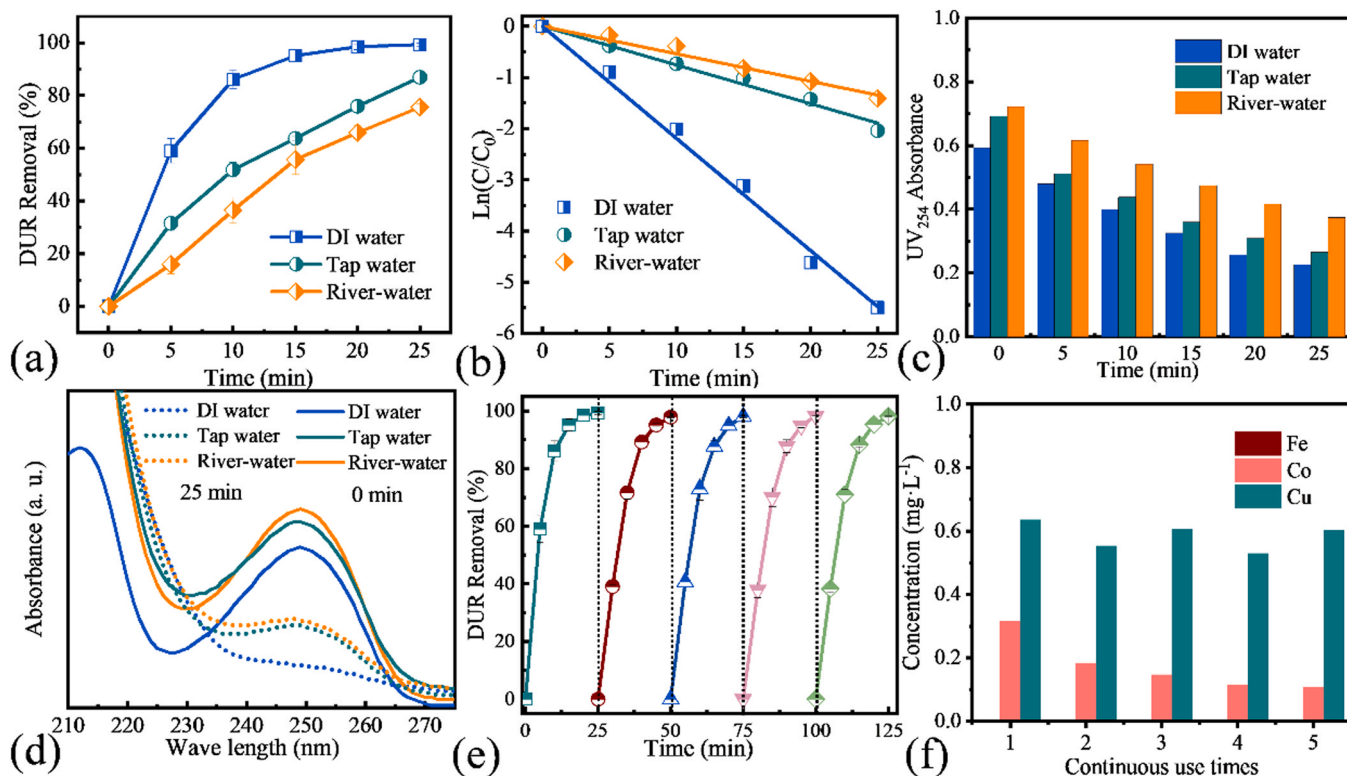


Fig. 7. The water matrix effect on DUR removal efficiency (a), removal rate (b), UV₂₅₄ (c), and ultraviolet absorption spectrum of samples (210–280 nm) (d). Degradation trend of DUR in DBDP/CFOC (e) and leaching concentration of metal ions (f).

3.3. Possible degradation mechanism analysis

3.3.1. Identification of active species

Experiments evidence has confirmed the DBDP/CFOC ability in DUR removal, but the mechanism in the elimination procedure needs to be investigated detailed. Reactive species in DBDP and DBDP/CFOC were detected via EPR detection with the help of DMPO and TEMP. As shown in Fig. 8a, the characteristic signal of DMPO- \bullet OH (with peaks separation of 45 Gauss) and TEMP- $^1\text{O}_2$ signal (with peaks separation of 30 Gauss) were detected [38]. In addition, the signals for pronated DMPO (DMPO-H) (with peaks separation of 80 Gauss) marked plum blossom were attributed to hydrated electrons [39,40]. Apparently, compared with DBDP, TEMP- $^1\text{O}_2$ signals in DBDP/CFOC performed a higher intensity. The EPR spectra indicated that CFOC might help the formation $^1\text{O}_2$. Molecule probes conducted further quantitative determination (1, 3-diphenylisobenzofuran (DPBF) for $^1\text{O}_2$ and Benzoic acid for \bullet OH [41]. The concentration evolution of $^1\text{O}_2$ and \bullet OH with time prolonged were depicted in Fig. 8b. Compared with DBDP, the yield of \bullet OH had no significant difference, but $^1\text{O}_2$ concentration increased by about 10 μM in DBDP/CFOC, which is consistent with EPR detection. $^1\text{O}_2$ could be produced from the interaction between \bullet OH and $\bullet\text{O}_2^-$ or from $\bullet\text{O}_2^-$ itself [31], and the addition of CFOC promote this procedure.

The contribution in DUR elimination of various reactive species was identified in radical-capture experiments performed by separately adding scavengers FFA, IPA, *p*-BQ, and AgNO_3 for $^1\text{O}_2$, \bullet OH, $\bullet\text{O}_2^-$, and e^-/\bullet H into simulated wastewater, respectively [9,42,43]. As shown in Fig. 8c, \bullet OH served as the major reactive species in the whole process of degradation in the DBDP process. However, in the DBDP/CFOC system, \bullet OH still plays a major role at the initial stage (< 5 min), but the contributions of $^1\text{O}_2$ and $\bullet\text{O}_2^-$ gradually appear with the extension of discharge treatment time. Since the input power was adjusted in 3.02 W in both systems, e^-/\bullet H contributed similarly to DUR elimination. This

phenomenon suggested that adding CFOC benefited the transformation of active species and DUR degradation through multipath. Further evidence could be found in Fig. 8d, the degradation rates of quenching experiments were calculated by pseudo-first-order reaction kinetics, and all coefficients (R^2) > 0.9. Inhibition efficiencies were calculated as Eq. (4) to reduce the different systems errors and evaluate the reactive species contribution [44]. ζ of various scavengers followed a sequence of $\text{IPA} > \text{AgNO}_3 \approx \text{FFA} > p\text{-BQ}$, implying that the contributions of reactive species on DUR elimination followed the sequence of $\bullet\text{OH} > e^-/\bullet\text{H} \approx ^1\text{O}_2 > \bullet\text{O}_2^-$ (Fig. 8e) in the DBDP system. However, with the addition of CFOC, the differences have been counterbalanced, and the reactive species in the system has been effectively utilized. It is speculated that CFOC might promote the generation of $\bullet\text{O}_2^-$ and $^1\text{O}_2$, and \bullet OH was no longer the advantaged effective species, which is consistent with EPR detection.

3.3.2. Mechanisms into DBDP activation for DUR elimination

To further investigate the catalyst mechanism in CFOC contribution to the $\bullet\text{O}_2^-$ and $^1\text{O}_2$ formation, DFT was applied in surface atomic structure models of crystal faces construction. The increased macroscopic plane of CuF in the substrate provides convenience for the adsorption of O_2 . As shown in Figs. 9a and 9b, the adsorption of O_2 on crystal faces changed the density of states in different atomic orbitals, and the bonding orbitals and the free electron distribution are affected. More straightforward electron transfer could be observed in the bond lengths of O-O. The derivatives of dioxygen have characteristic O-O distances that correlate with the bond state. Superoxide is a compound with an oxidation number of oxygen $-1/2$. Instead of having a double bond, in the ground-state dioxygen, diradical contains two unpaired electrons in dioxygen. Fig. 9d displays the bond lengths of O-O adsorbed on a crystal surface, the bond length of dioxygen increases from 1.222 Å to about 1.300 Å, which close to the distance of O-O in $\bullet\text{O}_2^-$ (1.332(2) Å)

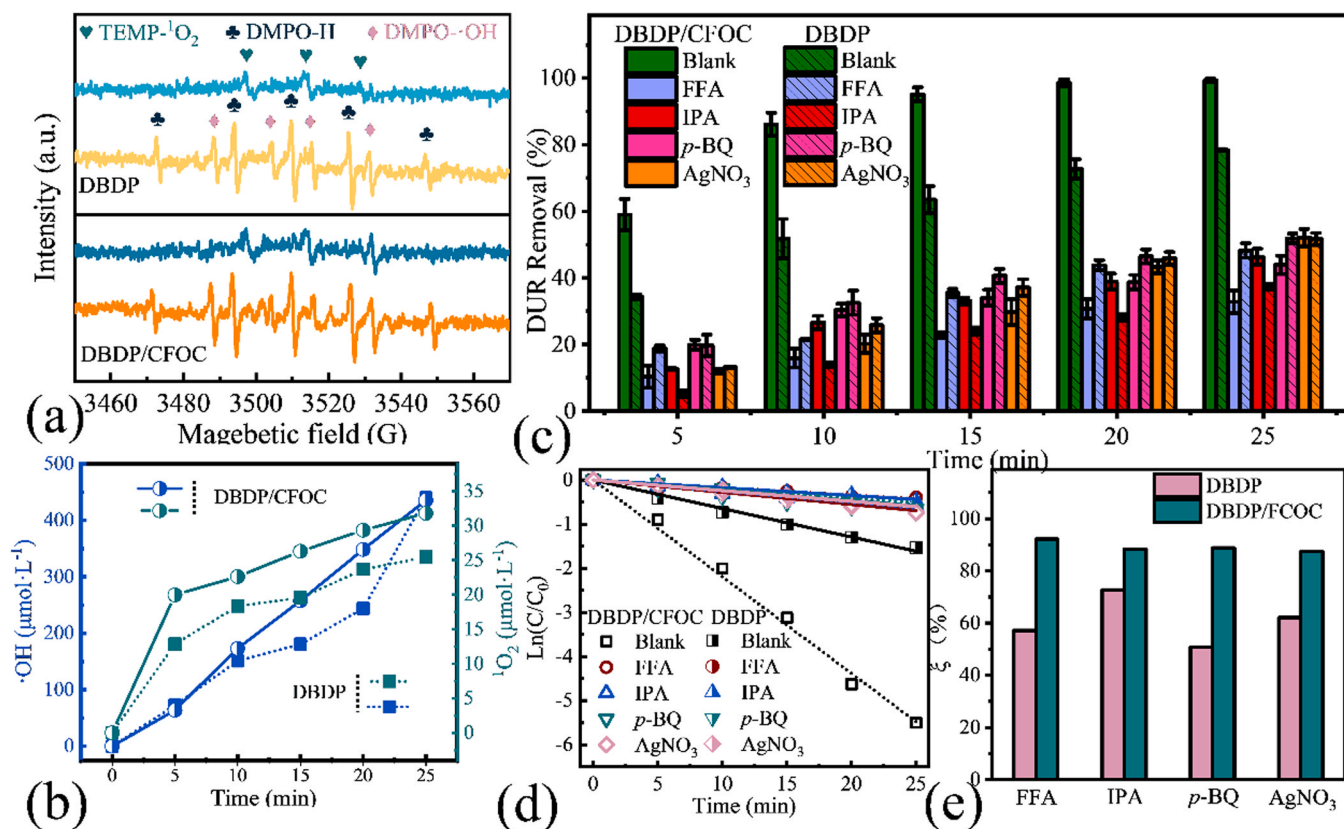


Fig. 8. EPR spectra for hydrated electron, \bullet OH and $^1\text{O}_2$ (a), active species concentration (b), DUR removal efficiency (c), scavenger effect on DUR removal rate (d), and ζ (e) in DBDP and DBDP/CFOC process.

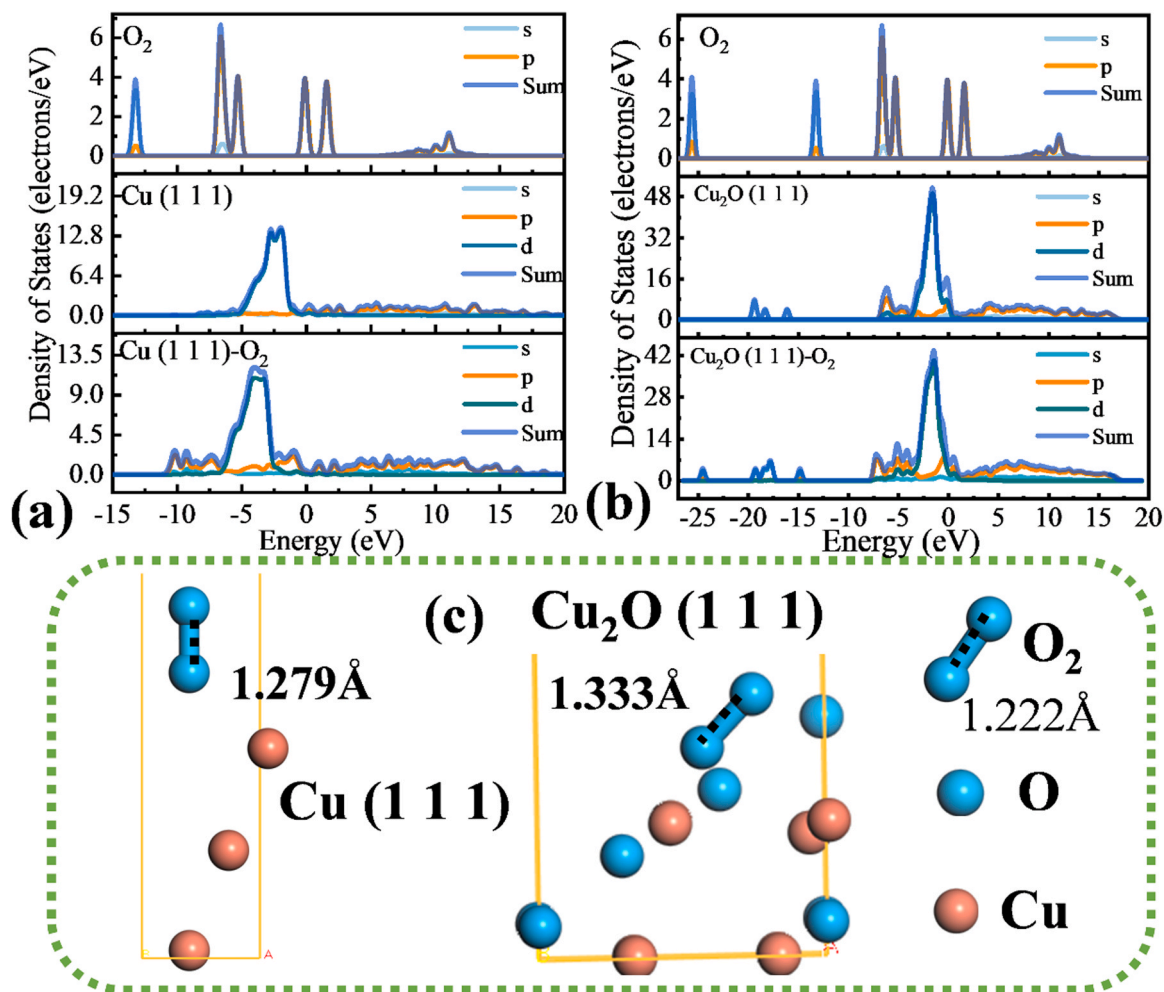
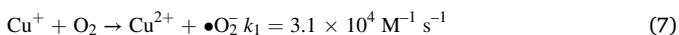


Fig. 9. Density of states in different atomic orbitals of O₂, Cu (1 1 1), Cu (1 1 1)-O₂ (a), O₂, Cu₂O (1 1 1), Cu₂O (1 1 1)-O₂ (b), and surface atomic structure models of crystal faces adsorb O₂ (c).

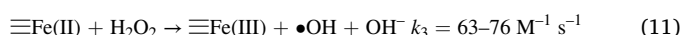
[45,46]. From these phenomena could infer that electron transfer occurs in the exposed crystal surface of CFOC during the adsorption of molecular oxygen, and the increase of O-O bond length may be activated to $\bullet\text{O}_2^-$. As shown in Eqs. (6–9), The elevation of $\bullet\text{O}_2^-$ yield was conducive to forming $^1\text{O}_2$ [9,47,48], which explains the phenomenon above that after adding CFOC, both the removal rate and other active species ($\bullet\text{O}_2^-$, $^1\text{O}_2$, and e^-) contribution in DUR removal increased.



XPS was adopted to explore the differences in valence state and oxygen species on the CFOC surface between fresh and recycled catalysts. Fig. 10 presents the XPS spectra, which are displayed in Table S5. The content of low-valence metals ($\equiv\text{Cu(I)}$) and O_A decreased on the CFOC surface after catalyzing DBDP. As shown in Eqs. (10–16), the catalysis of $\text{O}_3/\text{H}_2\text{O}_2$ depending on the electron transfer of surface metal ions [48–53]. The increased ratio of $\equiv\text{Co(II)}$ and $\equiv\text{Fe(II)}$ maintained the charge balance and ensured the catalytic cycle (Fig. 10b). However, the conversion of Fe(III) to Fe(II) depended on the Fenton self-reaction was too slow to comparative with Fe(II) consumption. The insights into valence transformation relied on the oxidation of $\equiv\text{Cu(I)} \rightarrow \equiv\text{Cu(II)}$ could recover the consumption of $\equiv\text{Fe(II)}$ in catalysis. Based on $\text{Fe}^{3+} +$

$\text{Cu}^+ \leftrightarrow \text{Fe}^{2+} + \text{Cu}^{2+}$ ($E^0(\text{Fe}^{3+}/\text{Fe}^{2+}) = 0.77 \text{ V}_{\text{NHE}}$, $E^0(\text{Cu}^{2+}/\text{Cu}^+) = 0.17 \text{ V}_{\text{NHE}}$), which benefit to the continuance of catalysis [52]. Also, the redox cycle occurred on Co, especially for Cu species expediting the mutual transformation according to the process of $\text{Co}^{3+} + \text{Cu}^+ \leftrightarrow \text{Co}^{2+} + \text{Cu}^{2+}$ ($E^0(\text{Co}^{3+}/\text{Co}^{2+}) = 1.81 \text{ V}_{\text{NHE}}$, $E^0(\text{Cu}^{2+}/\text{Cu}^+) = 0.17 \text{ V}_{\text{NHE}}$) [53]. The XPS results verified the electron transfer between variable metals, a vital pathway in oxidants activation and ROS production for processing DUR-containing water. As for the decrease of O_V , which mainly passes two pathways: i) Generating ROS by electron transfer; ii) maintaining charge balance, caused by low-valence metals consumption in DBDP catalysis: $-\text{M}^{(n+1)+} - \text{O}^{2-} - \text{M}^{(n+1)+} \leftrightarrow -\text{M}^{n+} - \square - \text{M}^{n+} - + 1/2 \text{ O}_2$ [54,55].

Based on the above results, the mechanisms for DBDP activation by CFOC are proposed, as shown in Fig. 10b. The superior catalysis properties performance of CFOC should be attributed to its unique structural characteristics as follows: i) the nanosheet stacked on the surface of CuF could optimize the transition metal (Co and Fe) catalytic sites exposure for the electron transport; ii) the carrier CuF reduce the resistance in electron transmit and Cu_2O formed in the calcination process conducive to O_2 activation; iii) low-valence Cu in quantity on the carrier CuF surface expedited the redox in metal irons and maintain the sustained catalytic activity. The scientific combination of active component and conductive carrier provides guarantee for catalytic activity.



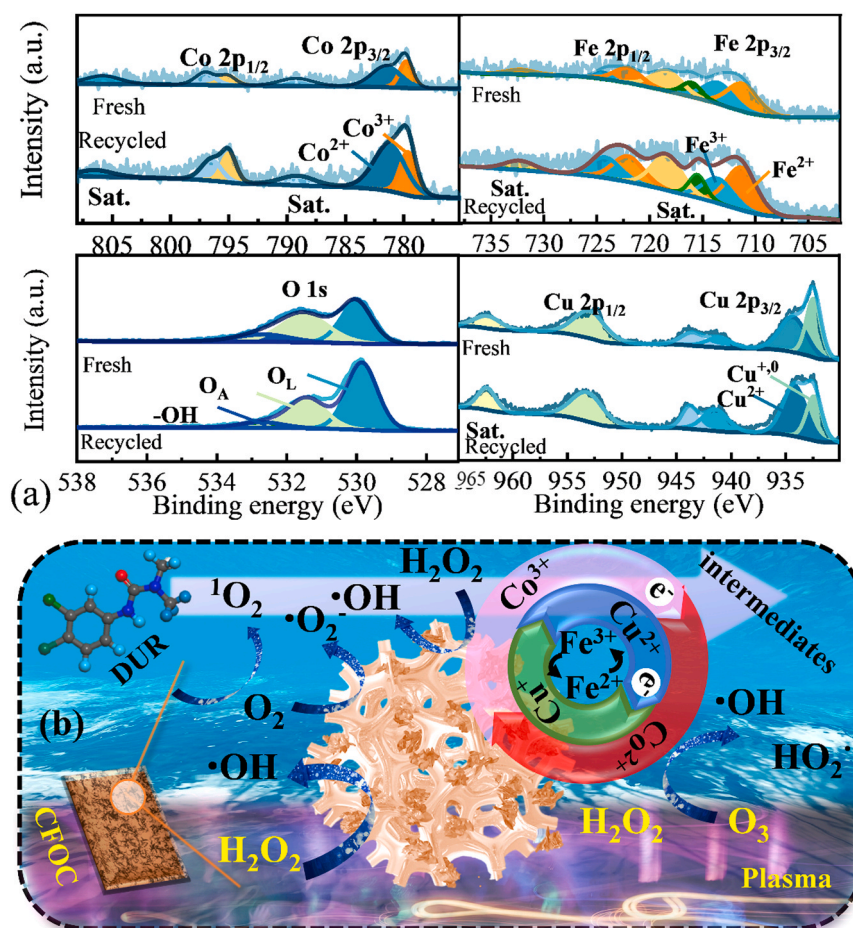
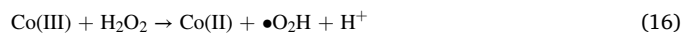
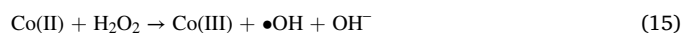
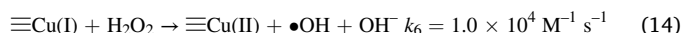
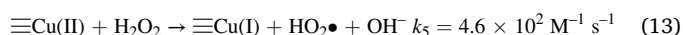
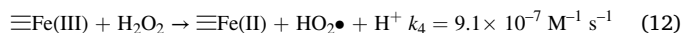


Fig. 10. XPS spectra of fresh and recycled CFOC, Co (2p), Fe (2p), O (1 s), and Cu (2p) (a). Mechanisms of DBDP activation catalyzed by CFOC (b).



3.3.3. Prediction of the possible DUR degradation pathway

To elucidate the transformation pathway of DUR in the DBDP/CFOC process, Q-TOF-LC/MS and DFT calculation was employed in intermediates detection [56]. During the destruction of DUR, a total of 18 transformation products were listed in Table S6, including their m/z and molecular structures. Combined with DFT calculation (Fig. S8), two evolution pathways were proposed in DUR degradation (Fig. 11): i) Cl (7) with high Fukui index ($f^- = 0.185$, $f^0 = 0.153$) was tended to be attacked by the electrophilic group and radicals, and the disintegration of DUR starts from dechlorinate (P1); ii) According to Mulliken population, the bonds of N(2)-C(9) (Length = 1.44 Å, Mulliken Population = 0.63) and N(2)-C(8) (Length = 1.45 Å, Mulliken Population = 0.62) have a longer length with a lower population, which more likely to be broken, and the disintegration of DUR starts from demethylation (P2). The electrostatic potential distribution map shows that the charge density is mainly concentrated in the N, Cl, and O atoms. Following the degradation initiation, under the attack of electrophilic groups and radicals, the intermediate product gradually degraded.

To further investigate the main degradation routes, except for small molecular fragments, the relative content of intermediates with aromatic structure is shown in Fig. 12. In both DBDP and DBDP/CFOC processes, the DUR degradation mainly along with P2→P6→P7→P8→P9. Dealkylation, alkylic-hydroxylation, and alkylic-oxidation reactions are the dominate routes to decompose DUR. The difference is that evolution progress in DBDP/CFOC system was more efficient than in DBDP. The C-centered radicals are readily attacked by ROS to form peroxide radical, which subsequently transforms into double-bond derivatives (P2), and the double-bond derivatives would evolve into dealkylation products (P7, P8, and P9) [57]. The other secondary degradation path is P1→P3→P4→P5, in which $\bullet\text{OH}$ continuously attacks Cl-C leading to the generation of dechlorination-hydroxylation (P1), and further oxidized by alkylic-hydroxylation (P3, P4, and P5).

Scavengers competed with pollutants for active species in the DBDP/CFOC process, and the proportion of intermediate products changed under the influence of quenching agents. As depicted in Fig. 12b, compared with the blank system, all the scavengers caused a decrease in the degradation ratio of DUR, which was consistent with the results in the identification of active species and suggested the participation of multiple substances ($^1\text{O}_2$, $\bullet\text{OH}$, $\text{e}^-/\bullet\text{H}$, and $\bullet\text{O}_2$) in DUR elimination. The scheme of dynamic species' possible action sites is displayed in Fig. 12c. When adding the FFA, the proportion of all intermediates except P6 and P7 decreased, indicating that further degradation pathway was blocked in the absence of $^1\text{O}_2$, resulting in P6 and P7 accumulation. The lack of $\bullet\text{OH}$ impacted P2 degradation, suggesting that the aldehyde group mainly relied on the oxidation of P2 by $\bullet\text{OH}$, which was converted to a carboxyl group and then decarboxylated to form P6. $\text{e}^-/\bullet\text{H}$ might benefit

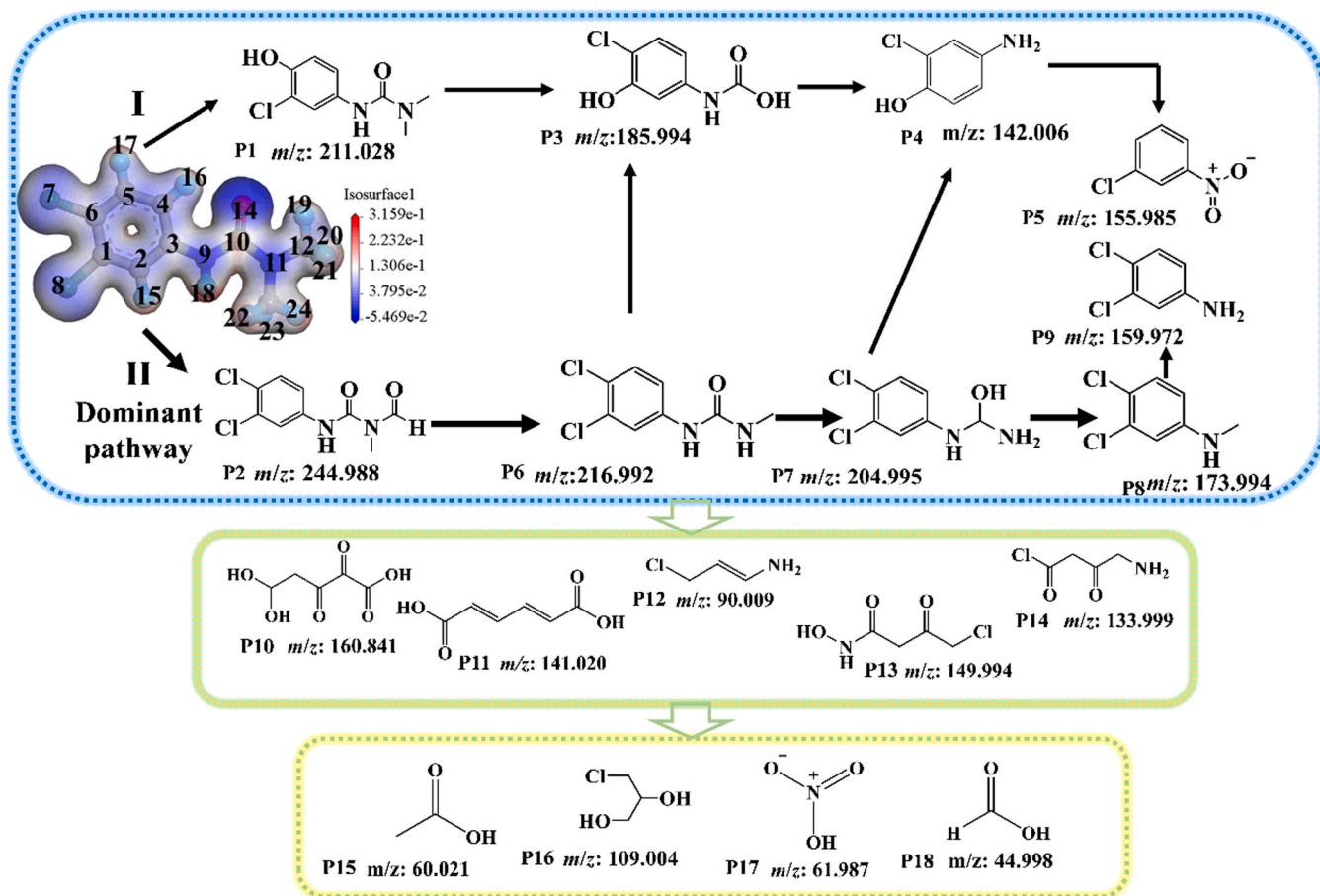


Fig. 11. Possible degradation pathway of DUR in DBDP/CFOC process.

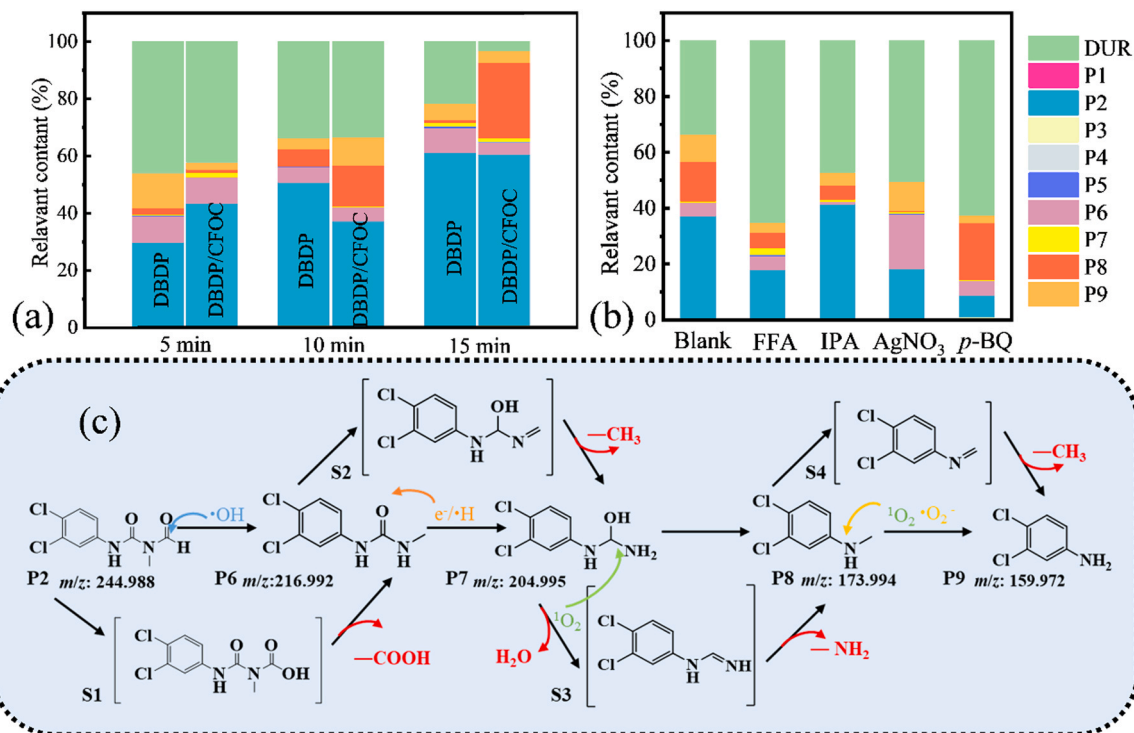


Fig. 12. The change of DUR intermediates fragments relevant content of LC-MS in DBDP and DBDP/CFOC process (at 5, 10 and 15 min) (a). Scavengers effect on relative molecular content of fragments (at 10 min) in DBDP/CFOC (b). The possible dominant DUR degradation process (c).

from the transition state of P6→P7, and the addition of AgNO₃ impedes the further degradation of P6. The attacking of •O₂ might induce dealkylation, and the decrement of •O₂ inhibited the demethylation of P8. Generally, the degradation process is like a disassembly line, and all these co-existing active species cooperatively disassemble the DUR efficiently.

3.4. Toxicity assessment of DUR degradation in DBDP/CFOC process based on QSAR

The environmental implications of DUR and intermediates were evaluated using Ecological Structure Activity Relationships (ECOSAR), which is based on the quantitative structure-activity relationship (QSAR) (Fig. 13). The *n*-octanol water partition coefficient (*K*_{ow}) is the ratio of the concentration of the compound in the *n*-octanol phase to the concentration in the water phase at equilibrium, which could measure the lipid solubility related to the solubility of intermediates, biological enrichment coefficient, and adsorption coefficient of soil and sediment. Thus, *K*_{ow} was applied to determine the migration, distribution, and direction of compounds in the environment. Most intermediates' acute and chronic toxicity towards fish, daphnia, and green algae were lower than those of DUR (Fig. 13a-f). Besides, the *K*_{ow} of intermediates was also reduced, suggesting the lipid solubility decreased, but migration and transformation activity increased (Fig. 13g). This eco-toxicological evaluation confirmed the environmentally-benign character of DBDP/CFOC.

CFOC.

4. Conclusions

In this work, a high catalytic activity ternary LDO was designed to enhance DBDP performance in DUR degradation by introducing CuF as an electron transport substrate. Credit to the synergistic effect of CFOC and DBDP, surface modification of LDO and Cu₂O significantly improved the energy efficiency and optimized the utilization of reactive species in DBDP by electron transport. As an electron transport substrate, CuF promotes the valence circulation (Fe(III)/Fe(II) and Co(III)/Co(II)), guaranteeing the catalysis sustainability and surface Cu₂O helping the generation of reactive oxygen species, and the ¹O₂ concentration increased by 10 μM. As a result, CFOC released the ability of ROS, and multiple reactive species cooperated to dismantle the DUR, increasing the energy yield of DUR degradation to 0.11 mg W⁻¹·min⁻¹ at 3.02 W. According to DFT calculation and Q-TOF-LC/MS detection, dealkylation, alkylic-hydroxylation, and alkylic-oxidation reactions were confirmed to be the possible dominant routes in DUR decomposition. Based on intermediate molecular structures, the quantitative structure-activity relationship (QSAR) predicted the toxicity decrease in the complete DBDP/CFOC process. The constructed DBDP/CFOC process might provide a new perspective in the field of catalyst synthesis and offer an effective consumption reduction strategy by exploiting the DBDP process's reactive species.

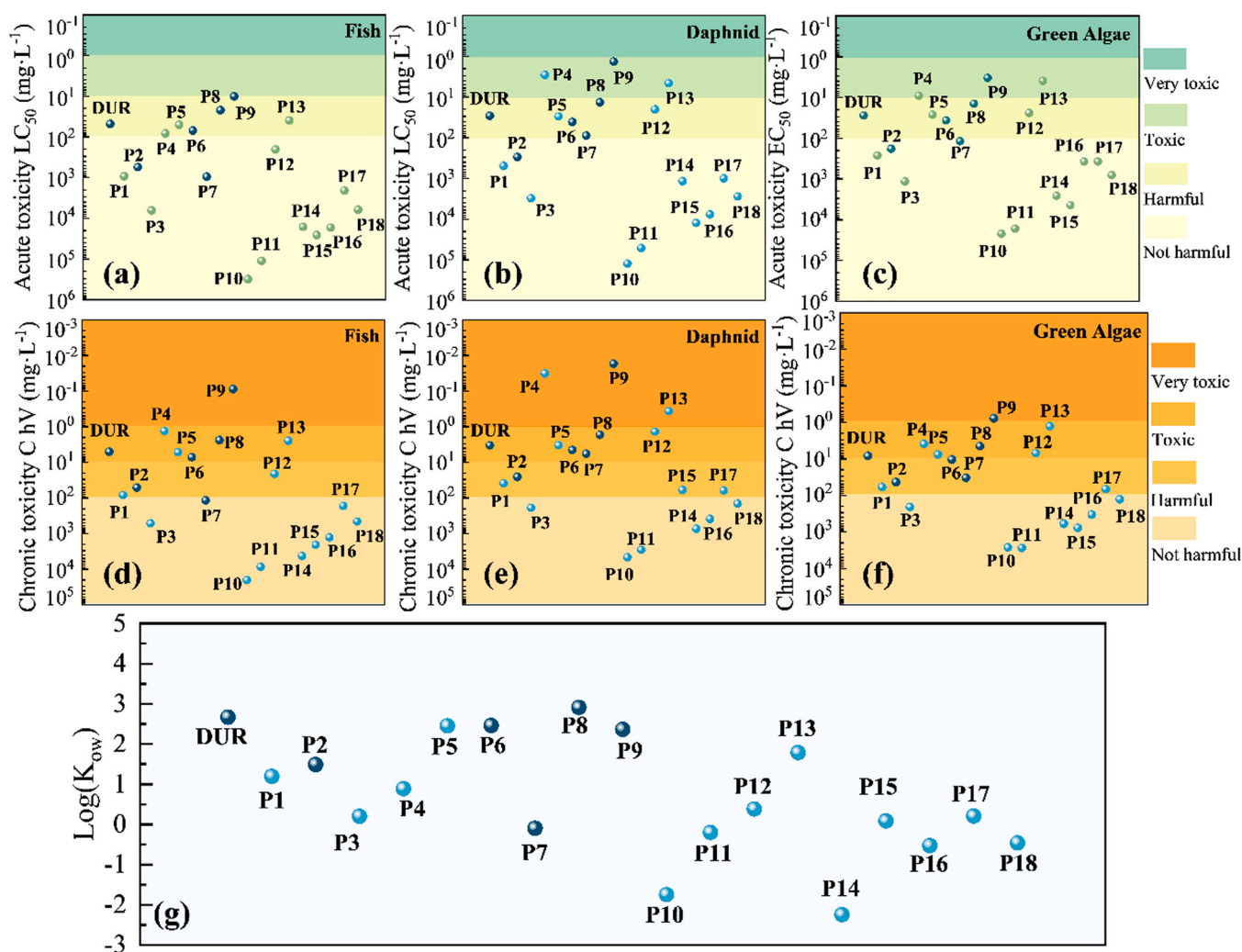


Fig. 13. Acute toxicity (a-c), chronic toxicity (d-f) and Log(*K*_{ow}) estimates of DUR with its intermediate products during degradation by DBDP/CFOC system via ECOSAR.

CRedit authorship contribution statement

Tianyao Shen: Conceptualization, Experimentalize, Data curation, Formal analysis, Investigation, Methodology, Validation, Writing – original draft. **Haihe Yu:** Writing – review & editing. **Peng Wang:** Funding acquisition, Project administration, Resources, Supervision. **Xiaoqing Wang:** Methodology, Investigation. **Chunyan Yang:** Writing – review & editing. **Peng Xu:** Data curation, Software. **Jianhua Qu:** Writing-review, Software. **Guangshan Zhang:** Investigation, Methodology, Writing – review & editing, Funding acquisition.

Declaration of Competing Interest

The authors declare that they have no known competing financial interests or personal relationships that could have appeared to influence the work reported in this paper.

Data availability

Data will be made available on request.

Acknowledgements

The work was supported by Natural Science Foundation of Shandong Province, China (ZR2022ME128), State Key Laboratory of Urban Water Resource and Environment (Harbin Institute of Technology) (2021TS02), and Talents of High Level Scientific Research Foundation of Qingdao Agricultural University (6651120004) for their financial support. Additional thanks go to the High Performance Computing Center, Harbin Institute of Technology.

Appendix A. Supporting information

Supplementary data associated with this article can be found in the online version at [doi:10.1016/j.apcatb.2023.122950](https://doi.org/10.1016/j.apcatb.2023.122950).

References

- [1] M. Tudi, H.D. Ruan, L. Wang, J. Lyu, R. Sadler, D. Connell, C. Chu, D.T. Phung, Agriculture development, pesticide application and its impact on the environment, *Int. J. Environ. Res. Public Health* 18 (2021) 1112, <https://doi.org/10.3390/ijerph18031112>.
- [2] J. Qu, Z. Li, Z. Wu, F. Bi, S. Wei, M. Dong, Q. Hu, Y. Wang, H. Yu, Y. Zhang, Cyclodextrin-functionalized magnetic alginate microspheres for synchronous removal of lead and bisphenol A from contaminated soil, *Chem. Eng. J.* 461 (2023), 142079, <https://doi.org/10.1016/j.cej.2023.142079>.
- [3] S. Sun, Y. Chen, Y. Lin, D. An, Occurrence, spatial distribution, and seasonal variation of emerging trace organic pollutants in source water for Shanghai, China, *Sci. Total Environ.* 639 (2018) 1–7, <https://doi.org/10.1016/j.scitotenv.2018.05.089>.
- [4] Y. Zhang, E.J. Calabrese, J. Zhang, D. Gao, M. Qin, Z. Lin, A trigger mechanism of herbicides to phytoplankton blooms: from the standpoint of hormesis involving cytochrome b559, reactive oxygen species and nitric oxide, *Water Res.* 173 (2020), 115584, <https://doi.org/10.1016/j.watres.2020.115584>.
- [5] J. Qu, R. Liu, X. Bi, Z. Li, K. Li, Q. Hu, X. Zhang, G. Zhang, S. Ma, Y. Zhang, Remediation of atrazine contaminated soil by microwave activated persulfate system: Performance, mechanism and DFT calculation, *J. Clean. Prod.* 399 (2023), 136546, <https://doi.org/10.1016/j.jclepro.2023.136546>.
- [6] T. Ke, L. Hu, L. Li, Q. Zheng, Y. Xin, G. Zhang, Recent advances in persulfate-based advanced oxidation processes for organic wastewater treatment, *Chin. Chem. Lett.* 33 (2022) 4461–4477, <https://doi.org/10.1016/j.ccl.2021.12.042>.
- [7] M. Magureanu, F. Bilea, C. Bradu, D. Hong, A review on non-thermal plasma treatment of water contaminated with antibiotics, *J. Hazard. Mater.* 417 (2021), 125481, <https://doi.org/10.1016/j.jhazmat.2021.125481>.
- [8] C.A. Aggelopoulos, Recent advances of cold plasma technology for water and soil remediation: a critical review, *Chem. Eng. J.* 428 (2022), 131657, <https://doi.org/10.1016/j.cej.2021.131657>.
- [9] K. Shang, R. Morent, N. Wang, Y. Wang, B. Peng, N. Jiang, N. Lu, J. Li, Degradation of sulfamethoxazole (SMX) by water falling film DBD Plasma/Persulfate: reactive species identification and their role in SMX degradation, *Chem. Eng. J.* 431 (2022), 133916, <https://doi.org/10.1016/j.cej.2021.133916>.
- [10] T. Shen, X. Wang, J. Li, P. Xu, C. Yang, P. Wang, G. Zhang, Introduction of oxygen vacancy to Bi₂Mn₄O₁₀ supported by nickel foam for ¹O₂ dominated metronidazole degradation under dielectric barrier discharge plasma, *Appl. Catal. B Environ.* 328 (2023), 122518, <https://doi.org/10.1016/j.apcatb.2023.122518>.
- [11] J. Lou, G. Lu, Y. Wei, Y. Zhang, J. An, M. Jia, M. Li, Enhanced degradation of residual potassium ethyl xanthate in mineral separation wastewater by dielectric barrier discharge plasma and peroxymonosulfate, *Sep. Purif. Technol.* 282 (2022), 119955, <https://doi.org/10.1016/j.seppur.2021.119955>.
- [12] X. Wang, Q. Huang, S. Ding, W. Liu, J. Mei, Y. Hunag, J. Luo, L. Lei, F. He, Micro hollow cathode excited dielectric barrier discharge (DBD) plasma bubble and the application in organic wastewater treatment, *Sep. Purif. Technol.* 240 (2020), 116659, <https://doi.org/10.1016/j.seppur.2020.116659>.
- [13] C.A. Aggelopoulos, S. Meropoulis, M. Hatzisymeon, Z.G. Lada, G. Rassias, Degradation of antibiotic enrofloxacin in water by gas-liquid nsp-DBD plasma: parametric analysis, effect of H₂O₂ and CaO₂ additives and exploration of degradation mechanisms, *Chem. Eng. J.* 398 (2020), 125622, <https://doi.org/10.1016/j.cej.2020.125622>.
- [14] H. Sun, N. Jiang, J. Ren, X. Wei, G. Yu, J. Li, Power dependence of reactive species generation in a water falling film dielectric barrier discharge system, *Sep. Purif. Technol.* 305 (2023), 122406, <https://doi.org/10.1016/j.seppur.2022.122406>.
- [15] Z. Yang, C. Zhang, G. Zeng, X. Tan, H. Wang, D. Huang, K. Yang, J. Wei, C. Ma, K. Nie, Design and engineering of layered double hydroxide based catalysts for water depollution by advanced oxidation processes: a review, *J. Mater. Chem. A* 8 (2020) 4141–4173, <https://doi.org/10.1039/C9TA13522G>.
- [16] S. Jatav, M. Herber, H. Xiang, E.H. Hill, Layered double hydroxide-bismuth molybdate hybrids toward water remediation via selective adsorption of anionic species, *ACS Appl. Mater. Interfaces* 14 (2022) 51921–51930, <https://doi.org/10.1021/acsami.2c14979>.
- [17] T.H. Kim, L.J. Young, J. Xie, P.J. Hoon, J.M. Oh, Topology dependent modification of layered double hydroxide for therapeutic and diagnostic platform, *Adv. Drug Deliv. Rev.* 188 (2022), 114459, <https://doi.org/10.1016/j.addr.2022.114459>.
- [18] A.K. Das, U.N. Pan, V. Sharma, N.H. Kim, J.H. Lee, Nanostructured CeO₂/NiV-LDH composite for energy storage in asymmetric supercapacitor and as methanol oxidation electrocatalyst, *Chem. Eng. J.* 417 (2021), 128019, <https://doi.org/10.1016/j.cej.2020.128019>.
- [19] B. Zhang, J. Wang, Z. Xu, S. Wu, R. Luque, H. Zhang, Sewage sludge valorisation by hydrothermal carbonization: a new method to enhance nitrogen removal in hydrochar catalyzed with Ni-Mg-Al layered double oxides, *J. Clean. Prod.* 386 (2023), 135880, <https://doi.org/10.1016/j.jclepro.2023.135880>.
- [20] V.R.L. Constantino, T.J. Pinnavaia, Basic properties of Mg²⁺-Al³⁺ layered double hydroxides intercalated by carbonate, hydroxide, chloride, and sulfate anions, *Inorg. Chem.* 34 (1995) 883–892, <https://doi.org/10.1002/in.199525006>.
- [21] Z. Wang, Y. Chen, X. Li, G. He, J. Ma, H. He, Layered double hydroxide catalysts for ozone decomposition: the synergic role of M²⁺ and M³⁺, *Environ. Sci. Technol.* 56 (2022) 1386–1394, <https://doi.org/10.1021/acs.est.1c07829>.
- [22] G. Peng, M. Xiang, W. Wang, Z. Su, H. Liu, Y. Mao, Y. Chen, P. Zhang, Engineering 3D graphene-like carbon-assembled layered double oxide for efficient microplastic removal in a wide pH range, *J. Hazard. Mater.* 433 (2022), 128672, <https://doi.org/10.1016/j.jhazmat.2022.128672>.
- [23] L. Zhang, Y.T. Ma, J.J. Duan, Y.Q. Yao, J.J. Feng, A.J. Wang, In-situ construction of 3D hetero-structured sulfur-doped nanoflower-like FeNi LDH decorated with NiCo Prussian blue analogue cubes as efficient electrocatalysts for boosting oxygen evolution reaction, *J. Colloid Interface Sci.* 611 (2022) 205–214, <https://doi.org/10.1016/j.jcis.2021.12.066>.
- [24] T. Shen, X. Wang, J. Li, C. Yang, P. Xu, H. Chai, P. Wang, G. Zhang, Construction of 3D ternary layered double hydroxides on nickel foam for enhancing dielectric barrier discharge plasma to degrade DUR: performance, mechanism and energy efficiency, *Chem. Eng. J.* 455 (2023), 140790, <https://doi.org/10.1016/j.cej.2022.140790>.
- [25] Y. Liu, X. Liu, Y. Zhao, D.D. Dionysiou, Aligned α-FeOOH nanorods anchored on a graphene oxide-carbon nanotubes aerogel can serve as an effective Fenton-like oxidation catalyst, *Appl. Catal. B Environ.* 213 (2017) 74–86, <https://doi.org/10.1016/j.apcatb.2017.05.019>.
- [26] X. Yao, Q. Lin, L. Zeng, J. Xiang, G. Yin, Q. Liu, Degradation of humic acid using hydrogen peroxide activated by CuO-Co₃O₄@AC under microwave irradiation, *Chem. Eng. J.* 330 (2017) 783–791, <https://doi.org/10.1016/j.cej.2017.08.008>.
- [27] P. Wang, J. Zhao, Q. Zhao, X. Ma, X. Du, X. Hao, B. Tang, A. Abudula, G. Guan, Microwave-assisted synthesis of manganese oxide catalysts for total toluene oxidation, *J. Colloid Interface Sci.* 607 (2022) 100–110, <https://doi.org/10.1016/j.jcis.2021.08.170>.
- [28] J. Qu, Y. Xu, X. Zhang, M. Sun, Y. Tao, X. Zhang, G. Zhang, C. Ge, Y. Zhang, Ball milling-assisted preparation of N-doped biochar loaded with ferrous sulfide as persulfate activator for phenol degradation: multiple active sites-triggered radical/non-radical mechanism, *Appl. Catal. B Environ.* 316 (2022), 121639, <https://doi.org/10.1016/j.apcatb.2022.121639>.
- [29] B. Palanivel, M.S. Hossain, C. Ayappan, V. Krishnan, R. Marnadu, T. Kalavani, F. A. Alharthi, G. Sreedevi, Activation of persulfate for improved naproxen degradation using FeCo₂O₄@g-C₃N₄ heterojunction photocatalysts, *ACS Omega* 6 (2021) 34563–34571, <https://doi.org/10.1021/acsomega.1c04896>.
- [30] P. Xu, R. Wei, P. Wang, X. Li, C. Yang, T. Shen, T. Zheng, G. Zhang, CuFe₂O₄/diatomite actuates peroxymonosulfate activation process: mechanism for active species transformation and pesticide degradation, *Water Res.* 235 (2023), 119843, <https://doi.org/10.1016/j.watres.2023.119843>.
- [31] Z. Guan, Y. Guo, Z. Mo, S. Chen, J. Liang, X. Liao, Y. Zhang, Z. Huang, W. Song, Y. Xu, X. Ou, S. Sun, High-efficiency treatment of electroless nickel plating effluent using core-shell MnFe₂O₄-C@Al₂O₃ combined with ozonation: performance and mechanism, *J. Hazard. Mater.* 433 (2022), 128768, <https://doi.org/10.1016/j.jhazmat.2022.128768>.

- [32] H. Ren, H. Liu, T. Cui, S. Liu, T. Ma, Z. Han, R. Zhou, Boosting the activation of peroxymonosulfate and the degradation of metronidazole over FeCo_2O_4 quantum dots anchored on $\beta\text{-FeOOH}$ nanosheets: inspired from octahedral Co(II) with missing angle, *Chem. Eng. J.* 431 (2022), 133803, <https://doi.org/10.1016/j.cej.2021.133803>.
- [33] J. Li, G. Gou, H. Zhao, C. Liu, N. Li, L. Li, B. Tan, B. Lai, Efficient peroxymonosulfate activation by $\text{CoFe}_2\text{O}_4\text{-CeO}_2$ composite: performance and catalytic mechanism, *Chem. Eng. J.* 435 (2022), 134840, <https://doi.org/10.1016/j.cej.2022.134840>.
- [34] P. Guha, B. Mohanty, R. Thapa, R.M. Kadam, P.V. Satyam, B.K. Jena, Defect-engineered MoO_2 nanostructures as an efficient electrocatalyst for oxygen evolution reaction, *ACS Appl. Energy Mater.* 3 (2020) 5208–5218, <https://doi.org/10.1021/acsomega.1c04896>.
- [35] S. Lu, G. Wang, S. Chen, H. Yu, F. Ye, X. Quan, Heterogeneous activation of peroxymonosulfate by $\text{LaCo}_{1-x}\text{Cu}_x\text{O}_3$ perovskites for degradation of organic pollutants, *J. Hazard. Mater.* 353 (2018) 401–409, <https://doi.org/10.1016/j.jhazmat.2018.04.021>.
- [36] J. Ren, N. Jiang, K. Shang, N. Lu, J. Li, Y. Wu, Synergistic degradation of trans-ferric acid by water falling film DBD plasma coupled with cobalt oxyhydroxide: performance and mechanisms, *Chem. Eng. J.* 372 (2019) 321–331, <https://doi.org/10.1016/j.cej.2019.04.147>.
- [37] C. Wang, J. Zhang, J. Du, P. Zhang, Z. Zhao, W. Shi, F. Cui, Rapid degradation of norfloxacin by $\text{VUV/Fe}^{2+}/\text{H}_2\text{O}_2$ over a wide initial pH: process parameters, synergistic mechanism, and influencing factors, *J. Hazard. Mater.* 416 (2021), 125893, <https://doi.org/10.1016/j.jhazmat.2021.125893>.
- [38] J. Qu, X. Tian, X. Zhang, J. Yao, J. Xue, K. Li, B. Zhang, L. Wang, Y. Zhang, Free radicals-triggered reductive and oxidative degradation of highly chlorinated compounds via regulation of heat-activated persulfate by low-molecular-weight organic acids, *Appl. Catal. B Environ.* 310 (2022) 1, <https://doi.org/10.1016/j.apcatb.2022.121359>.
- [39] Z. Chen, C. Li, J. Gao, H. Dong, Y. Chen, B. Wu, C. Gu, Efficient reductive destruction of perfluoroalkyl substances under self-assembled micelle confinement, *Environ. Sci. Technol.* 54 (2020) 5178–5185, <https://doi.org/10.1021/acs.est.9b06599>.
- [40] K.P. Madden, H. Taniguchi, In situ radiolysis time-resolved esr studies of spin trapping by DMPO: reevaluation of hydroxyl radical and hydrated electron trapping rates and spin adduct yields, *J. Phys. Chem.* 100 (1996) 7511–7516, <https://doi.org/10.1021/jp953382h>.
- [41] W. Zheng, S. You, Y. Yao, L. Jin, Y. Liu, Development of atomic hydrogen-mediated electrocatalytic filtration system for peroxymonosulfate activation towards ultrafast degradation of emerging organic contaminants, *Appl. Catal. B Environ.* 298 (2021), 120593, <https://doi.org/10.1016/j.apcatb.2021.120593>.
- [42] D. Zhu, Z. Sun, H. Zhang, A. Zhang, Y. Zhang, A.C. Miruka, L. Zhu, R. Li, Y. Guo, Y. Liu, Reactive nitrogen species generated by gas-liquid dielectric barrier discharge for efficient degradation of perfluorooctanoic acid from water, *Environ. Sci. Technol.* 56 (2022) 349–360, <https://doi.org/10.1021/acs.est.1c06342>.
- [43] T. Shen, K. Tian, M. Cao, L. Li, F. Shi, J. Qu, Q. Zheng, G. Zhang, Application of nickel foam supported Cu-MnO_2 in microwave enhanced Fenton-like process for p-nitrophenol removal: degradation, synergy and mechanism insight, *J. Clean. Prod.* 397 (2023), 136442, <https://doi.org/10.1016/j.jclepro.2023.136442>.
- [44] A. Zhang, Y. Zhou, Y. Li, Y. Liu, X. Li, G. Xue, A.C. Miruka, M. Zheng, Y. Liu, Motivation of reactive oxygen and nitrogen species by a novel non-thermal plasma coupled with calcium peroxide system for synergistic removal of sulfamethoxazole in waste activated sludge, *Water Res.* 212 (2022), 118128, <https://doi.org/10.1016/j.watres.2022.118128>.
- [45] P.D.C. Dietzel, R.K. Kremer, M. Jansen, Tetraorganylammonium superoxide compounds: close to unperturbed superoxide ions in the solid state, *J. Am. Chem. Soc.* 126 (2004) 4689–4696, <https://doi.org/10.1021/ja039880i>.
- [46] X. Tao, C.G. Daniliuc, O. Janka, R. Pottgen, R. Knitsch, M.R. Hansen, H. Eckert, M. Lubbesmeyer, A. Studer, G. Kehr, G. Erker, Reduction of dioxygen by radical/B ($\text{p-C}_6\text{F}_4\text{X}$)₃ pairs to give isolable bis(borane)superoxide compounds, *Angew. Chem. Int. Ed. Engl.* 56 (2017) 16641–16644, <https://doi.org/10.1002/anie.201709309>.
- [47] X. Li, J. Liu, A.I. Rykov, H. Han, C. Jin, X. Liu, J. Wang, Excellent photo-Fenton catalysts of Fe–Co Prussian blue analogues and their reaction mechanism study, *Appl. Catal. B Environ.* 179 (2015) 196–205, <https://doi.org/10.1016/j.apcatb.2015.05.033>.
- [48] H. Lee, H. Lee, J. Seo, H. Kim, Y.K. Shin, J. Kim, C. Lee, Activation of oxygen and hydrogen peroxide by copper(II) coupled with hydroxylamine for oxidation of organic contaminants, *Environ. Sci. Technol.* 50 (2016) 8231–8238, <https://doi.org/10.1021/acs.est.6b02067>.
- [49] C. Dong, J. Ji, B. Shen, M. Xing, J. Zhang, Enhancement of H_2O_2 decomposition by the co-catalytic effect of WS_2 on the Fenton reaction for the synchronous reduction of Cr(VI) and remediation of phenol, *Environ. Sci. Technol.* 52 (2018) 11297–11308, <https://doi.org/10.1021/acs.est.8b02403>.
- [50] A.D. Bokare, W. Choi, Review of iron-free Fenton-like systems for activating H_2O_2 in advanced oxidation processes, *J. Hazard. Mater.* 275 (2014) 121–135, <https://doi.org/10.1016/j.jhazmat.2014.04.054>.
- [51] J. Weinstein-Lloyd, S.E. Schwartz, Low-intensity radiolysis study of free-radical reactions in cloudwater: hydrogen peroxide production and destruction, *Environ. Sci. Technol.* 25 (1991) 791–800, <https://doi.org/10.1021/es00016a027>.
- [52] S. Xin, B. Ma, C. Zhang, X. Ma, P. Xu, G. Zhang, M. Gao, Y. Xin, Catalytic activation of peroxydisulfate by alfalfa-derived nitrogen self-doped porous carbon supported CuFeO_2 for nimesulide degradation: Performance, mechanism and DFT calculation, *Appl. Catal. B Environ.* 294 (2021), 120247, <https://doi.org/10.1016/j.apcatb.2021.120247>.
- [53] X. Guo, B. Hu, K. Wang, H. Wang, B. Li, M. Guo, Y. Tian, R. Zhang, S. Shi, Y. Han, Cu embedded Co oxides and its fenton-like activity for metronidazole degradation over a wide pH range: active sites of Cu doped Co_3O_4 with {112} exposed facet, *Chem. Eng. J.* 435 (2022), 132910, <https://doi.org/10.1016/j.cej.2021.132910>.
- [54] X. Wang, X. Li, J. Mu, S. Fan, X. Chen, L. Wang, Z. Yin, M. Tadé, S. Liu, Oxygen vacancy-rich porous Co_3O_4 nanosheets toward boosted NO reduction by CO and CO oxidation: insights into the structure–activity relationship and performance enhancement mechanism, *ACS Appl. Mater. Interfaces* 11 (2019) 41988–41999, <https://doi.org/10.1021/acsami.9b08664>.
- [55] C. Dong, Z. Qu, X. Jiang, Y. Ren, Tuning oxygen vacancy concentration of MnO_2 through metal doping for improved toluene oxidation, *J. Hazard. Mater.* 391 (2020), 122181, <https://doi.org/10.1016/j.jhazmat.2020.122181>.
- [56] P. Xu, X. Li, R. Wei, C. Yang, T. Shen, P. Wang, G. Zhang, High adaptability and stability FeCo_2O_4 /diatomite composite for efficient peroxymonosulfate activation: performance, water matrix impact, and mechanism, *Chem. Eng. J.* 462 (2023), 142204, <https://doi.org/10.1016/j.cej.2023.142204>.
- [57] C. Li, Y. Huang, X. Dong, Z. Sun, X. Duan, B. Ren, S. Zheng, D.D. Dionysiou, Highly efficient activation of peroxymonosulfate by natural negatively-charged kaolinite with abundant hydroxyl groups for the degradation of atrazine, *Appl. Catal. B Environ.* 247 (2019) 10–23, <https://doi.org/10.1016/j.apcatb.2019.01.079>.